Local Flow Measurements of Vertical Upward Bubbly Flow in an Annulus

Takashi Hibiki [a, b, *], Rong Situ [b], Ye Mi [b], Mamoru Ishii [b]

[a] *Research Reactor Institute, Kyoto University, Kumatori, Sennan, Osaka 590-0494, Japan*

[b] *School of Nuclear Engineering, Purdue University, West Lafayette, IN 47907-1290, USA*

* Tel: +81-724-51-2373, Fax.: +81-724-51-2461, Email: hibiki@rri.kyoto-u.ac.jp

Abstract

Local measurements of flow parameters were performed for vertical upward bubbly flows in an annulus. The annulus channel consisted of an inner rod with a diameter of 19.1 mm and an outer round tube with an inner diameter of 38.1 mm, and the hydraulic equivalent diameter was 19.1 mm. Double-sensor conductivity probe was used for measuring void fraction, interfacial area concentration, and interfacial velocity, and Laser Doppler anemometer was utilized for measuring liquid velocity and turbulence intensity. A total of 20 data sets for void fraction, interfacial area concentration, and interfacial velocity were acquired consisting of five void fractions, about 0.050, 0.10, 0.15, 0.20, and 0.25, and four superficial liquid velocities, 0.272, 0.516, 1.03, and 2.08 m/s. A total of 8 data sets for liquid velocity and turbulence intensity were acquired consisting of five void fractions, about 0.050, and 0.10, and four superficial liquid velocities, 0.272, 0.516, 1.03, and 2.08 m/s. The constitutive equations for distribution parameter and drift velocity in the drift-flux model, and the semi-theoretical correlation for Sauter mean diameter namely interfacial area

concentration, which were proposed previously, were validated by local flow parameters obtained in the experiment using the annulus.

Key Words: Void fraction, Interfacial area concentration; Bubble size; Liquid velocity; Turbulence intensity; Double-sensor conductivity probe; Laser Doppler anemometer; Drift-flux model; Gas-liquid bubbly flow; Multiphase flow; Annulus

Nomenclature

A	coefficient
a_{i}	interfacial area concentration
$a_{\mathrm{i,c}}$	interfacial area concentration of cap bubble
C_0	distribution parameter
$C_{0\infty}$	asymptotic value of C_0
C_{D}	drag coefficient for a multi-particle system
$C_{\mathrm{D}\infty}$	drag coefficient for a single particle
D	diameter of round tube
D_{b}	bubble diameter or diameter of small bubbles
D_{c}	diameter of cap bubbles
D_{H}	hydraulic equivalent diameter
D_{Sm}	Sauter mean diameter
$\widetilde{D}_{\mathrm{Sm}}$	non-dimensional Sauter mean diameter
d_{f}	fringe spacing
f_{total}	calibration factor
g	gravitational acceleration
j	mixture volumetric flux
j_{g}	superficial gas velocity
$j_{\mathrm{g,N}}$	superficial gas velocity reduced at normal condition (atmospheric pressure and 20°C)
j_{f}	superficial liquid velocity
Lo	Laplace length

$\widetilde{Lo}$	non-dimensional Laplace length
N_{b}	number of total bubbles detected
N_{miss}	number of missing bubbles
n	exponent
P	pressure
R	radius of outer round tube
R_0	radius of inner rod
Re	Reynolds number
Re_{f}	Reynolds number of liquid phase
r	radial coordinate
r_{P}	radial coordinate at the void peak
u_{x}	fluid velocity
V_{gj}	void fraction-weighted mean drift velocity
v_{g}	interfacial velocity obtained by effective signals
v_{gj}	local drift velocity
v'_{g}	fluctuation of interfacial velocity
v_{f}	liquid velocity
$v_{\mathrm{f,max}}$	maximum liquid velocity
x	beam direction
y	coordinate normal to beam direction
z	axial coordinate

Greek symbols

α	void fraction
α_{C}	void fraction at the channel center

α_c	void fraction of cap bubble
α_P	void fraction at the void peak
Δd	probe traversing distance
Δr	actual location change of measurement volume
Δs	distance between two tips of sensors
ΔT	total sampling time at a local point
Δt_j	time delay obtained by effective signals for j-th bubble interface
$\Delta\rho$	density difference
ε	energy dissipation rate per unit mass
$\widetilde{\varepsilon}$	non-dimensional energy dissipation rate per unit mass
κ	half of angle between the dual beams
λ	wavelength of laser beam
μ_f	liquid viscosity
μ_g	gas viscosity
ν_f	kinematic liquid viscosity
ρ_g	gas density
ρ_f	liquid density
ρ_m	mixture density
σ	interfacial tension

Subscripts

calc.	calculated value
meas.	measured value
γ-densitometer	quantity measured by a γ-densitometer

Mathematical symbols

< >	area-averaged quantity
<< >>	void fraction weighted cross-sectional area-averaged quantity

1. Introduction

The range of two-phase flow applications in today's technology is immense. State-of-the-art computer systems demand high-heat flux, low temperature gradient cooling of electronic circuits which can only be satisfied by boiling systems. Chemical engineering applications desire optimization of chemical processes when bubbling gases into liquid solutions. In these situations knowledge of the gas-liquid interface conditions is paramount for determining their reaction kinetics. In this case, the necessary transport of the gas into a liquid phase can limit the productivity of a process. Advanced nuclear reactor concepts rely on the extremely high heat removal only possible through liquid boiling. Since small changes in local parameters such as flow quality can drastically change the flow conditions in steam-water systems, it is indispensable to understand two-phase flow behavior in order to produce reliable accident-safety calculations. In addition, all large-scale power production facilities rely on steam production for driving steam turbine generators. For all of the above situations, an uncertainty in design arises from the lack of fundamental understanding of the hydrodynamics and processes which determine critical parameters such as fluid particle sizes and interfacial areas. Therefore, future technology has clearly presented the need for a better understanding of the nature of two-phase flows.

The basic structure of a bubbly two-phase flow can be characterized by two fundamental geometrical parameters. These are the void fraction and interfacial area concentration. The void fraction expresses the phase distribution and is a required parameter for hydrodynamic and thermal design in various industrial processes. On the other hand, the interfacial area describes available area for the interfacial transfer of mass, momentum and energy, and is a required parameter for a two-fluid model formulation. Various transfer mechanisms between phases depend on the two-phase interfacial structures. Therefore, an

accurate knowledge of these parameters is necessary for any two-phase flow analyses. This fact can be further substantiated with respect to two-phase flow formulation.

In view of the great importance to two-fluid model, local measurement of these flow parameters such as void fraction and interfacial area concentration have been performed in a bubbly flow intensively over the past 10 years [1-12]. However, most of experiments were performed in round tubes. In relation to the core cooling of a light water reactor (LWR), critical heat flux in an internally heated annulus has been investigated by many researchers [13], but very little data base is available for local flow parameters of two-phase bubbly flow in an annulus. From this point of view, this study aims at measuring local flow parameters of vertical upward air-water bubbly flows in an annulus. The annulus test loop is scaled to a prototypic BWR based on scaling criteria for geometric, hydrodynamic, and thermal similarities [14]. It consists of an inner rod with a diameter of 19.1 mm and an outer round tube with an inner diameter of 38.1 mm, and the hydraulic equivalent diameter is 19.1 mm. Measured flow parameters include void fraction, interfacial area concentration, interfacial velocity, liquid velocity and turbulence intensity. Double-sensor conductivity probe, and Laser Doppler anemometer are used for measuring local flow parameters of gas and liquid flows, respectively. A total of 20 data sets for local flow parameters of the gas phase are acquired consisting of five void fractions, about 0.050, 0.10, 0.15, 0.20, and 0.25, and four superficial liquid velocities, 0.272, 0.516, 1.03, and 2.08 m/s. A total of 8 data sets for local flow parameters of the liquid phase are acquired consisting of five void fractions, about 0.050 and 0.10, and four superficial liquid velocities, 0.272, 0.516, 1.03, and 2.08 m/s. The constitutive equations for distribution parameter and drift velocity in the drift-flux model, and the semi-theoretical correlation for Sauter mean diameter namely interfacial area concentration, which were previously proposed by the present authors, are validated by local flow parameters obtained in this experiment using the annulus.

2. Experimental

2.1. Double sensor probe methodology

Local flow parameters such as void fraction, interfacial area concentration, and interfacial velocity were measured by a double-sensor conductivity probe [15, 16]. The double-sensor conductivity probe is used basically as a phase identifier of the two-phase mixture. The double-sensor conductivity probe consists of two sensors made of stainless steel acupuncture needles with its maximum outer diameter of 0.10 mm. The two wires are adjusted for typical distance of approximately 1.5 mm in the length wise direction and are aligned in the axial direction. The information to be recorded from each signal are the number of bubbles that have hit the sensor, the time that the sensor is exposed to the gas phase, and the relative time between the bubble hitting the upstream and downstream sensor. The time-averaged interfacial velocity, v_g, is calculated by taking into account the distance between the tips of the upstream and downstream sensor and the time difference between the upstream and downstream signal. The time-averaged void fraction, α, is simply the accumulated time the sensor is exposed to the gas phase divided by the total sampling time of the sensor. It has been shown mathematically that the interfacial area concentration, a_i, equals the harmonic mean of the interfacial velocity [15]. The theoretical base of this measurement technique was given by Kataoka et al. [15]. Recently, Wu and Ishii [17] pointed out that a small spherical bubble might miss one sensor of the double-sensor conductivity probe. In what follows, their correction method accounting for the missed interfaces of spherical bubbles in the application of the double-sensor conductivity probe will be described in detail [17, 18].

Wu and Ishii [17] considered the effects of the lateral movement of the bubbles and the probe tip spacing. They divided the measured bubbles in two categories, one for bubbles whose interface was moving normal to the probe and passing through both the sensors, and another for those missing one of the sensors of the probe. In their correction scheme, the mean value of the experimentally measured bubble interfacial velocity was rigorously related to the actual interfacial velocity of the bubbles by defining theoretical calibration factors. These calibration factors were employed to account for the bubbles whose interfaces moved normal to the probe, and those missing one of the sensors. By determining the calibration factors, they modified the formula given by Kataoka et al. [15] as

$$a_i = f_{total}\left(\frac{2N_b}{\Delta s \Delta T}\right)\left(\frac{\sum_j \Delta t_j}{N_b - N_{miss}}\right), \quad \text{for } \Delta s=0.36D_b\sim0.86D_b \tag{1}$$

with

$$f_{total} = 2+\left(\frac{v_g'}{v_g}\right)^{2.25}, \quad \text{for } \Delta s=0.36D_b\sim0.86D_b \tag{2}$$

where f_{total}, N_b, Δs, ΔT, Δt_j, N_{miss}, D_b, v_g', and v_g are the calibration factor, the number of total bubbles detected, the distance between two tips of the sensors, the total sampling time at a local point, the time delay obtained by effective signals for j-th bubble interface, the number of missing bubbles, the bubble diameter, and the fluctuation of the interfacial velocity, and the interfacial velocity obtained by effective signals, respectively. Equation (1) was found to be valid as long as the output signals from the probe were valid for bubble identification and the sample size was sufficiently large. For bubble sizes varying from 0.6 to 1.4 times the mean bubble size, it was found that the interfacial area concentration calculated by Eq.(1) would result in a statistical error of $\pm$7 % for a sample size of ~1000 bubbles [17].

In the strict sense, the assumption of spherical bubbles may not be valid for any bubbly flow systems. Bubble shapes in the present experiment may be ellipsoidal with wobbling interfaces. However, it is considered that the assumption of spherical bubbles would practically work for the interfacial area concentration measurement on the following grounds. In the previous study [10], the area-averaged interfacial area concentrations measured by the double-sensor conductivity probe method were compared with those measured by a photographic method in relatively low void fraction ($<\alpha>\leq 8$ %) and wide superficial liquid velocity (0.262 m/s $\leq <j_f> \leq$ 3.49 m/s) conditions where the photographic method could be applied. Here, < > indicates the area-averaged quantity. Good agreement was obtained between them with an averaged relative deviation of ±6.95 % [11]. In addition to this, when a spherical bubble is transformed into an ellipsoidal bubble with the aspect ratio of 2, the resulting increase of the interfacial area is estimated mathematically to be less than 10 % [19].

Using a fast A/D converter Keithly-Metrabyte DAS-1801HC board, local flow measurements were conducted in a data acquisition program. The acquisition board has a maximum sampling rate of 333,000 cycles per second. For the data sets measured with the double-sensor conductivity probe, a minimum of 2000 bubbles were sampled to maintain similar statistics between the different combinations of gas flow rates. Here, in the void fraction measurement at bubbly-to-slug flow transition, bubbles can be separated into either a cap bubble or a small bubble based on the double-sensor conductivity probe signals [12, 20]. The determination whether detected bubbles are cap bubbles is performed based upon the chord length of bubbles. According to Ishii and Zuber [21], the boundary between distorted and spherical-cap bubbles is given by $4(\sigma/g\Delta\rho)^{0.5}$, which corresponds to the bubble diameter of 10.9 mm in an air-water system at 20 °C. In the present experiment, when local bubble chord length exceeded this value, bubbles were considered as cap bubbles. Thus, the void

fraction for each category was obtained by the double-sensor conductivity probe separately. It should be noted here that the signals for cap bubbles were not acquired in the measurement of the interfacial area concentration, $a_{i,c}$, as well as the Sauter mean diameter, D_c, but the void fraction, α_c. The Sauter mean diameter in the high void fraction region where cap bubbles appeared was calculated from $D_{Sm}=6\alpha/a_i \approx 6\alpha/(a_i-a_{i,c})$, since the contribution of cap bubbles to total interfacial area concentration would be relatively small; for example, $a_{i,c}/a_i=4.76$ % for $\alpha_c/\alpha=0.2$ and $D_c/D_b=5$ [11]. In the present experiment, the number of cap bubbles was not significant even for high void fraction region. Thus, even Sauter mean diameter might be able to be approximated by $6(\alpha-\alpha_c)/(a_i-a_{i,c})$. The double-sensor conductivity probe methodology was detailed in the previous paper [10, 11, 16, 19, 20].

It should be noted here that the double-sensor conductivity probe method may not work in the vicinity of a wall. The presence of the wall doesn't allow a bubble to pass the probe randomly as in the other positions in the channel. This fact will cause a measurement error in the interfacial area concentration, and interfacial velocity in the vicinity of the wall. The detailed discussion was given by Kalkach-Navarro [4]. The range where the double-sensor conductivity probe method can work may roughly be estimated as $D_b/D_H \le r/(R-R_0) \le 1-D_b/D_H$, where r, R, R_0, and D_H are the radial distance measured from the inner rod surface, the inner radius of the outer round tube, the radius of the inner rod, and the hydraulic equivalent diameter, respectively. In this experiment (D_H=19.1 mm), the effective range of the double-sensor conductivity probe may roughly be estimated to be $0.10 \le r/(R-R_0) \le 0.90$ or $0.16 \le r/(R-R_0) \le 0.84$ for D_b=2 or 3 mm, respectively. However, the upstream probe can work well for the measurement of the void fraction and the number of bubbles which pass the point per unit time. As will be explained later, the local interfacial velocities can be fitted by the following function.

$$v_g = \frac{n+1}{n}\langle v_g \rangle \left\{ 1 - \left| \frac{2r - (R - R_0)}{R - R_0} \right| \right\}^{1/n}, \quad (3)$$

where n is the exponent. For most of bubbly flows [10], the calibration factor, f_{total}, can be approximated to be 2. Therefore, some data of the interfacial area concentration close to the wall where the double-sensor conductivity probe may not work well were calculated from the void fraction and the number of bubbles which passed the point per unit time measured by the front probe, the interfacial velocity estimated by Eq.(3), and Eq.(1).

2.2. Laser Doppler anemometer methodology

Local flow parameters such as liquid velocity, and turbulence intensity were measured by Laser Doppler anemometer (LDA) [22,23]. LDA is one of the most productive instruments for flow velocity measurements. The dual-beam approach is the most common optical arrangement used for an LDA system. The intersection of two laser beams from a common source defines the region from which measurements can be conducted. The actual measurement region may be a subset of the beam intersection reduced by the field of view of the receiver optics and the detection limits of the signal processor. Particles crossing the measurement region scatter light that is collected by a receiver probe. The light signal is converted to an electrical "Doppler burst" signal with a frequency related to the particle velocity. The method is shown in Fig.1, where λ, κ, and d_f are the wavelength of the laser beam, half of the angle between the dual beams, and the fringe spacing, respectively. The fluid velocity, u_x, is the product of d_f and the frequency of the proto-detector signal.

As shown in Fig.2, an integrated LDA system, consisting of an argon-ion laser, a multicolor beam separator (Model 9201 ColourBurst), a multicolor receiver (Model 9230 ColorLink), a signal processor (IFA 550), a fiberoptic probe (Model 9253-350), a personal

computer, and an software (FIND for Windows), was used in the liquid velocity measurement. The argon-ion laser has a maximum power of 100 mW. The focal length of the lens in the fiber-optic probe is 350 mm. The photo-detector is placed inside of the fiber probe, and it captures the back-scattered laser beam. A small amount of seeding TiO_2 particles with an average diameter of about 2 μm were added into the liquid to serve as the scattering centers for the laser beam and generally follow the main flow. The Photo-Multiplier-Tube (PMT) voltage setting was in the range of 1100 to 1200. In the gas-liquid two-phase bubble flow, large particles, such as bubbles, also scatter or reflect laser light, and the burst signals from the scattered light may also be interpreted as effective velocity information by the system. To avoid this effect, our experiments were only conducted under single-phase flow and two-phase flow with void fraction less than 0.1. Thus, only less than 10 percent of the received signals are from bubble scattering. In the experiment, more than 2000 data points can be obtained in the bulk region in 30 seconds. However, at the region close to the wall (heater rod or tube wall), the counting rate is relatively low. One reason is that most of the seeding particles flow in the bulk region. The other reason is that the measuring region is ellipsoid-shaped, and the measured length is 1.31 mm. When the focal region is very close to the wall (less than 1 mm), some portion of the measuring region is out of boundary. This will significantly reduce the counting rate. In the present experiment, at each location around the boundary region, data was taken for 90 seconds or more, and at each location around the bulk region, data was taken for 30 seconds.

The LDA probe was traversing normal to the test section. In what follows, the determination of measuring position will be discussed. For an annular channel, the laser beam will be refracted two times when it passes the tube wall. Both the beam direction and focal length will be changed. Figure 3 shows how to adjust the focus position. A laser probe is put in front of the test section tube. Laser beams coming out from the probe pass

through the transparent tube wall, and focus on a point where the fluid passes through. During a test, the focus position will be traversed on the cord AB, as shown in Fig.3(a). The laser beams are tangential to the heater rod. Some part of the beams may touch the heater rod. The laser intensity after laser beams pass point B is reduced. This is why the measurement was conducted in the region of AB, instead of B. Traversing the focus position on line EF is not accepted because the heater rod will reflect the laser beam and interfere the measurement. Moving the probe in *y* direction is also not a suitable option. When the probe is moving in *y* direction, the focus position and laser direction are both changed because of the round geometry of the flow channel. Among all the options, moving the probe in *x* direction to make the focus position on line AB is the best choice because the probe is moved in the same direction as the laser beam, and the beam direction and beam distance to the heater rod (DB) are not changed.

The sequences of determining the measurement position are:

(1) Move the laser probe so that laser beams pass through the flow channel without hitting the heater rod;

(2) Move the laser probe in *y* direction until it is tangential at the heater rod;

(3) Move the probe outside a little bit so that beams are not hindered by the heat rod;

(4) Move the probe backward until the focus point is at the close end of the inner wall, position *A'* in Fig.3, and record the position by reading the micrometer;

(5) Move the probe forward until focus point is at the far end of the inner wall, position *A'* in Fig.3, and record this position;

(6) Calculate the center position of cord *A'C'* , point D, and the cord length *A'C'*;

(7) Calculate the distance from the cord *A'C'* to the heater rod surface, DB;

(8) Move the probe in y direction toward the heat rod with the distance of DB so that the beams are tangential to the heater rod at point B;

(9) Calculate the cord length AC;

(10) Calculate the positions of the probe corresponding to the certain non-dimensional radius of focus points. It should be noted here that because the refractive index difference between water and air, the actual location change of measurement volume, Δr, is not same as the probe traversing distance Δd. The refractive index of water and the polycarbonate tube are 1.33 and 1.66, respectively.

During the test, a very small angle between the direction of the probe and the traverse system were found. In order to deal with this problem, first, the probe was moved backward or forward to find the actual locations of heater boundary and tube boundary by checking the LDA signal. Second, assuming that the focus position is traversing on the line between these two boundaries, the angle between beam and traverse direction was calculated, and the real non-dimensional radius was also calculated. The LDA methodology was detailed in the previous paper [22,23].

2.3. Two-phase flow experiment

An experimental facility was designed to measure the relevant two-phase parameters necessary for developing constitutive models for the two-fluid model in subcooled boiling. It was scaled to a prototypic BWR based on scaling criteria for geometric, hydrodynamic, and thermal similarities [14]. The experimental facility, instrumentation, and data acquisition system are briefly described in this section [14].

The two-phase flow experiment was performed by using a flow loop constructed at Thermal-Hydraulics and Reactor Safety Laboratory in Purdue University. Figure 4 shows

the experimental facility layout. The water supply is held in the holding tank. The tank is open to the atmosphere through a heat exchanger mounted to the top to prevent explosion or collapse and to degas from the water. There is a cartridge heater inside the tank to heat the water and maintain the inlet water temperature. A cooling line runs inside the tank to provide control of the inlet water temperature and post-experimental cooling of the tank. Water is pumped with a positive displacement, eccentric screw pump, capable of providing a constant head with minimum pressure oscillation. The water, which flows through a magnetic flow meter, is divided into four separate flows and can then be mixed with air before it is injected into the test section to study adiabatic air-water bubbly flow. For the adiabatic air-water flow experiment, porous spargers with the pore size of 10 μm are used as air injectors. The test section is an annular geometry that is formed by a clear polycarbonate tube on the outside and a cartridge heater on the inside. The test section is 38.1 mm inner diameter and has a 3.18 mm wall thickness. The overall length of the heater is 2670 mm and has a 19.1 mm outer diameter. The heated section of the heater rod is 1730 mm long. The maximum power of the heater is 20 kW and has a maximum surface heat flux of 0.193 MW/m^2. The heater rod has one thermocouple that is connected to the process controller to provide feedback control. The heater rod can be traversed vertically to allow many axial locations to be studied with four instrument ports attached to the test section. At each port there is an electrical conductivity probe. A pressure tap and thermocouple are placed at the inlet and exit of the test section. A differential pressure cell is connected between the inlet and outlet pressure taps. The loop can also be operated with a diabatic steam-water flow in a future study. The two-phase mixture flows out of the test section to a separator tank and the gas phase is piped away and the water is returned to the holding tank.

The flow rates of the air and water were measured with a rotameter and a magnetic flow meter, respectively. The loop temperature was kept at a constant temperature (20 °C)

within the deviation of ±0.2 °C by a heat exchanger installed in a water reservoir. The local flow measurements using the LDA were performed at an axial location of z/D_H=49.8 and thirteen radial locations from $r/(R-R_0)$=0.025 to 0.975. The local flow measurements using the double-sensor conductivity probe were performed at two axial locations of z/D_H=40.3 and 61.7 and ten radial locations from $r/(R-R_0)$=0.05 to 0.9. To compare the gas flow measurements with the liquid flow measurements, flow parameters for the gas phase measured at z/D_H=40.3 and 61.7 were averaged to estimate those at z/D_H=51.0, where was very close to the axial position for liquid flow measurements (z/D_H=49.8). A γ–densitometer was installed at z/D_H=51.1 in the loop to measure the area-averaged void fraction. The flow conditions in this experiment are tabulated in Table 1. The area-averaged superficial gas velocities in this experiment were roughly determined so as to provide the same area-averaged void fractions among different conditions of superficial liquid velocity, namely $<\alpha>$=0.050, 0.10, 0.15, 0.20, and 0.25. As explained in section 2.2, a small amount of seeding TiO_2 particles with an average diameter of about 2 μm were added into the liquid to serve as the scattering centers for the laser beam. However, as shown in Fig.5, the seeding particles did not affect the local flow measurements.

In order to verify the accuracy of local measurements, the area-averaged quantities obtained by integrating the local flow parameters over the flow channel were compared with those measured by other cross-calibration methods such as a γ-densitometer for void fraction, a photographic method for interfacial area concentration, a rotameter for superficial gas velocity, and a magnetic flow meter for superficial liquid velocity. Area-averaged superficial gas velocity was obtained from local void fraction and gas velocity measured by the double-sensor conductivity probe, whereas area-averaged superficial liquid velocity was obtained from local void fraction measured by the double-sensor conductivity probe and local liquid velocity measured by the LDA. Good agreements were obtained between the

area-averaged void fraction, interfacial area concentration, superficial gas velocity, and superficial liquid velocity obtained from the local measurements and those measured by the γ-densitometer, the photographic method, the rotameter, and the magnetic flow meter with averaged relative deviations of ±12.8 [24], ±6.95 [11], ±12.9 %, and ±15.5 %, respectively.

3. Results and discussion

3.1. Local flow parameters

3.1.1. Local flow parameters in gas phase

Figures 6, 7, 8, and 9 show the behavior of void fraction, interfacial area concentration, interfacial velocity, and Sauter mean diameter profiles measured in this experiment. The meanings of the symbols in these figures are found in Table 1. As can be seen from Fig.6, various phase distribution patterns similar to those in round tubes were observed in the present experiment, and void fraction profiles were found to be almost symmetrical with respect to the channel center, $r/(R\text{-}R_0)$=0.5. Serizawa and Kataoka classified the phase distribution pattern into four basic types of the distributions, that is, "wall peak", "intermediate peak", "core peak", and "transition" [1]. The wall peak is characterized as sharp peak with relatively high void fraction near the channel wall and plateau with very low void fraction around the channel center. The intermediate peak is explained as broad peak in void fraction near the channel wall and plateau with medium void fraction around the channel center. The core peak is defined as broad peak around the channel center and no peak near the channel wall. The transition is described as two broad peaks around the channel wall and center. In Fig.10, non-dimensional peak void fraction (upper figures) and

peak radial position (lower figures) are plotted against the area-averaged void fraction as a parameter of the superficial liquid velocity. The non-dimensional void fraction at the peak is defined as $(\alpha_P-\alpha_C)/\alpha_P$, where α_P and α_C are the void fraction at the peak and the channel center, respectively. $(\alpha_P-\alpha_C)/\alpha_P=0$ and 1 indicate no wall peak and very sharp wall peak, respectively. The non-dimensional radial position at the peak is defined as $r_P/(R-R_0)$, where r_P is the peak radial position. The left and right figures are the data measured for peaks appeared at inner and outer sides of the channel, respectively.

As the superficial liquid velocity increased, the radial position at the void fraction peak was moved towards the channel wall. The increase in the superficial liquid velocity also augmented the void fraction at the peak and made the void fraction peak sharp. On the other hand, in the present experimental condition, the increase in the void fraction did not change the radial position at the void fraction peak significantly, and decreased the non-dimensional void fraction at the peak, resulting in the broad void fraction peak. As general trends observed in the present experiment, the increase in the superficial liquid velocity decreased the bubble size, whereas the increase in the void fraction increased the bubble size. It was pointed out that the bubble size and liquid velocity profile would affect the void fraction distribution. Similar phenomena were also observed by Sekoguchi et al. [25], Zun [26], and Serizawa and Kataoka [1]. Sekoguchi et al. [25] observed the behaviors of isolated bubbles, which were introduced into vertical water flow in a 25 mm × 50 mm rectangular channel through a single nozzle. Based on their observations, they found that the bubble behaviors in dilute suspension flow might depend on the bubble size and the bubble shape. In their experiment, only distorted ellipsoidal bubbles with a diameter smaller than nearly 5 mm tended to migrate toward the wall, whereas distorted ellipsoidal bubbles with a diameter larger than 5 mm and spherical bubbles rose in the channel center. On the other hand, for the water velocity lower than 0.3 m/s, no bubbles were observed in the wall region.

Zun [26] also obtained a similar result. Zun performed an experiment to study void fraction radial profiles in upward vertical bubbly flow at very low average void fractions, around 0.5 %. In his experiment, the wall void peaking flow regime existed both in laminar and turbulent bulk liquid flow. The experimental results on turbulent bulk liquid flow at Reynolds number near 1000 showed distinctive higher bubble concentration at the wall region if the bubble equivalent sphere diameter appeared in the range of 0.8 and 3.6 mm. Intermediate void profiles were observed at bubble sizes either between 0.6 and 0.8 mm or 3.6 and 5.1 mm. Bubbles smaller than 0.6 mm or larger than 5.1 mm tended to migrate towards at the channel center. Thus, these experimental results suggested that the bubble size would play a dominant role in void fraction profiles. Serizawa and Kataoka [1] also gave an extensive review on the bubble behaviors in bubbly-flow regime.

Figure 11 shows a map of phase distribution patterns observed in this experiment. The open symbols of circle, triangle, and square in Fig.11 indicate the wall peak, the intermediate peak, and the core peak, respectively. The transition was not observed in this experiment. Since Serizawa and Kataoka [1] did not give the quantitative definitions of the wall and intermediate peaks, the classification between the wall and intermediate peaks in the present study were performed as the wall peak for $(\alpha_P-\alpha_C)/\alpha_P \geq 0.5$ and the intermediate peak for $(\alpha_P-\alpha_C)/\alpha_P<0.5$. For $<j_f>=0.272$ m/s and void fraction lower than 0.10, the void fraction profiles were almost uniform along the channel radius with some decrease in size near the wall, and such void fraction profiles were categorized as the core peak in this experiment. The solid and broken lines in Fig.11 are, respectively, the flow regime transition boundaries predicted by the model of Taitel et al. [27] and the phase distribution pattern transition boundaries, which were developed by Serizawa and Kataoka [1] based on experiments performed by different researchers with different types of bubble injections in round tubes (20 mm $\leq D \leq$ 86.4 mm). A fairly good agreement was obtained between the

Serizawa-Kataoka's map [1] and observed phase distribution patterns except for low superficial liquid velocity. As can be seen from Fig.4, the void fraction profiles for $\langle j_f \rangle$=0.272 m/s, were almost uniform along the radius with relatively steep decrease in the void fraction close to wall. This may be attributed to strong mixing due to bubble-induced turbulence, since it would dominate the flow in such a low flow condition. The strong mixing and partly recirculation would make the void fraction profile flatter. The similar void fraction peak was observed in the previous experiment using a 50.8 mm diameter pipe [23]. In the experiment, for $\langle j_f \rangle$=5.00 m/s, not the intermediate peak suggested by the Serizawa-Kataoka's map [25] but the flat peak characterized as uniform void fraction profile along the channel radius with relatively steep decrease in the void fraction near the wall was observed. The shear-induced turbulence would dominate the flow in such a high flow condition. It was considered that the reason for the phase distribution might be due to a strong bubble mixing over the flow channel by a strong turbulence. Thus, low and high liquid velocity regions may be considered to be bubble-mixing dominant zone, where the void fraction profile is uniform along the channel radius with relatively steep decrease in the void fraction near the wall. Thus, based on the phase distribution pattern, bubbly flow region may be divided into four regions: (1) bubble-mixing region where the bubble-induced turbulence is dominant, (2) region where the wall peak appears, (3) region where the core peak appears, and (4) bubble-mixing region where the shear-induced turbulence is dominant. The regions (1), (2), (3), and (4) are roughly located at low void fraction and low liquid velocity ($\langle \alpha \rangle \leq 0.25$, $\langle j_f \rangle \leq 0.3$ m/s), low void fraction and medium liquid velocity ($\langle \alpha \rangle \leq 0.25$, 0.3 m/s$\leq \langle j_f \rangle \leq$5 m/s), high void fraction ($\langle \alpha \rangle \geq 0.25$), and low void fraction and high liquid velocity($\langle \alpha \rangle \leq 0.25$, $\langle j_f \rangle \geq$5 m/s), respectively. Various transition phase distribution patterns would obviously appear between two regions. Intermediate peak and transition categorized by Serizawa and Kataoka may just be the transition between regions (4) and (2) or (3), and the transition

between regions (1) and (2) or (3), respectively.

Figure 9 shows the behavior of Sauter mean diameter profiles, corresponding to that of void fraction profiles in Fig. 6. The Sauter mean diameter profiles were almost uniform along the channel radius with some decrease in size near the wall, $r/(R\text{-}R_0)\leq 0.1$ and $0.9\leq r/(R\text{-}R_0)$. Only a part of a bubble can pass the region close to the channel wall, resulting in apparent small Sauter mean diameter.

Figure 7 shows the behavior of interfacial area concentration profiles, corresponding to that of void fraction profiles in Fig.6. As expected for bubbly flow, the interfacial area concentration profiles were similar to the void fraction profiles. Since the interfacial area concentration would directly be proportional to the void fraction and the Sauter mean diameter was almost uniform along the channel radius, the interfacial area concentration profiles displayed the same behavior as their respective void fraction profiles.

Figure 8 shows the behavior of interfacial velocity profiles, corresponding to that of void fraction profiles in Fig.6. As expected, the interfacial velocity had a power-law profile. As shown in Fig.8, measured interfacial velocities could be fitted by Eq.(3) reasonably well except for $<j_f>$=2.08 m/s and higher void fraction. Figure 12 shows the dependence of the exponent characterizing the interfacial velocity profile on the void fraction, $<\alpha>$, or the superficial liquid velocity, $<j_f>$. As the area-averaged void fraction increased, the exponent increased gradually, resulting in flatter interfacial velocity profile. As the superficial liquid velocity increased, the exponent decreased gradually and approached to the asymptotic value. Since the interfacial velocity would have the same tendency of the respective liquid velocity profile [12], the interfacial velocity profile might be attributed to the balance of the bubble-induced turbulence and shear-induced turbulence. It was observed in a round tube that for low liquid superficial velocities ($<j_f>\leq 1$ m/s) the introduction of bubbles into the liquid flow flattened the liquid velocity profile and the liquid velocity profile approached to

that of developed single-phase flow with the increase of void fraction [12]. It was also reported that the effect of the bubble introduction into the liquid on the liquid velocity profile was diminishing with increasing gas and liquid velocities and for high liquid velocities ($<j_f>\geq 1$ m/s) the liquid velocity profile came to be the power law profile as the flow developed. Thus, for low or high liquid velocity, the bubble-induced or shear-induced turbulence would play an important role in determining the liquid velocity profile, respectively.

3.1.2. Local flow parameters in liquid phase

Figures 13, and 14 show the behavior of liquid velocity, and turbulence intensity profiles corresponding to that of void fraction profiles in Fig.6. Here, turbulence intensity is defined as the ratio of liquid velocity to maximum liquid velocity. The meanings of the symbols in these figures are found in Table 1. In addition to these, the symbol of open circle means the value measured in a water single-phase flow. As shown in Fig.13, for low liquid velocities ($<j_f>$=0.272, 0.516, and 1.03 m/s), the introduction of bubbles into the liquid flow flattened the liquid velocity profile, with a relatively steep decrease close to the wall. The effect of the bubble on the liquid velocity profile appeared to be diminishing with increasing gas and liquid velocities. For high liquid velocity ($<j_f>$=2.08 m/s), the liquid velocity profile came to be the power-law profile similar to the liquid velocity profile observed in the single-phase flow.

As shown in Fig.14, the introduction of bubbles into the liquid flow will generally cause more agitated flow than in single-phase flow turbulence. As Serizawa and Kataoka [28] pointed out, under certain flow conditions, the two-phase flow turbulence is reduced locally by bubbles, when compared with single-phase flow turbulence intensity for the same liquid flow rate. They explained the enhancement and reduction of two-phase flow turbulence due to he bubble introduction as follows: (1) enhanced energy dissipation and

turbulence production in the wall region due to the large gradient of the velocity fluctuation and shear stress distribution there, (2) bubble relative motions which generate additional turbulence, (3) large velocity fluctuation gradient near gas-liquid interfaces increases turbulence energy dissipation, and (4) energy dumping effects of bubbles at interfaces. As shown in Fig.14, a slight turbulence intensity reduction phenomena in this experiment was observed locally for $<j_f>$=2.08 m/s and $<j_{g,N}>$=0.108 m/s (●; $<\alpha>$=0.0452). The similar results were also reported by Wang et al. [29], Hibiki and Ishii [11], and Hibiki et al. [12]. Serizawa and Kataoka [28] suggested that the turbulence reduction occurred roughly at liquid velocities higher than approximately 1 m/s. The present experimental result would support the Serizawa-Kataoka's observation. On the other hand, the turbulence intensity enhancement phenomenon was observed for $<\alpha>>0.05$ regardless of the liquid velocity [12].

The turbulence intensity profiles observed in this experiment were almost uniform along the radius with some increase near the wall for $<j_f>$=1.03 and 2.08 m/s or similar to intermediate peak explained in 3.1.2. for $<j_f>$=0.272 and 0.516 m/s. Michiyoshi and Serizawa [30] explained that this peaking in the wall region would reflect agitating bubble motions due to bubble-wall interactions and also the interactions between bubbles and large scale liquid eddies.

3.2 Drift-flux model

3.2.1. One-dimensional drift-flux model

The drift-flux model is one of the most practical and accurate models for two-phase flow. The model takes into account the relative motion between phases by a constitutive relation. It has been utilized to solve many engineering problems involving two-phase flow dynamics [31]. In particular, its application to forced convection systems has been quite successful. The one-dimensional drift-flux model is given by

$$\left\langle\left\langle v_g \right\rangle\right\rangle = \frac{\left\langle j_g \right\rangle}{\left\langle \alpha \right\rangle} = \frac{\left\langle \alpha j \right\rangle}{\left\langle \alpha \right\rangle\left\langle j \right\rangle}\left\langle j \right\rangle + \frac{\left\langle \alpha v_{gj} \right\rangle}{\left\langle \alpha \right\rangle} = C_0\left\langle j \right\rangle + V_{gj}, \tag{4}$$

where v_{gj}, C_0 and V_{gj} are the drift velocity of a gas phase defined as the velocity of the gas phase with respect to the volume center to the mixture, j, the distribution parameter defined by Eq.(5) and the void-fraction-weighted mean drift velocity defined by Eq.(6), respectively. << >> means the void-fraction-weighted mean value.

$$C_0 \equiv \frac{\left\langle \alpha j \right\rangle}{\left\langle \alpha \right\rangle\left\langle j \right\rangle}, \tag{5}$$

and

$$V_{gj} = \frac{\left\langle \alpha v_{gj} \right\rangle}{\left\langle \alpha \right\rangle}. \tag{6}$$

The void-fraction-weighted mean gas velocity, $<j_g>/<\alpha>$, and the cross-sectional mean mixture volumetric flux, $<j>$, are easily obtainable parameters in experiments. Therefore, Eq.(4) suggests a plot of $<j_g>/<\alpha>$ versus $<j>$. An important characteristic of such a plot is that, for two-phase flow regimes with fully-developed void and velocity profiles, the data points cluster around a straight line. The value of the distribution parameter, C_0, has been obtained indirectly from the slope of the line, whereas the intercept of this line with the void-fraction-weighted mean gas velocity axis can be interpreted as the void-fraction-weighted mean local drift velocity, V_{gj}. As recent development of local sensor techniques enables the measurement of the local flow parameters in a bubbly flow such as void fraction, and gas and liquid velocities, the values of C_0 and V_{gj} in a bubbly flow can be determined directly by Eqs.(5) and (6) from experimental data of the local flow parameters.

3.2.2. Constitutive equation of distribution parameter

Ishii [31] developed a simple correlation for the distribution parameter in

bubbly-flow regime. Ishii first considered a fully-developed bubbly flow and assumed that C_0 would depend on the density ratio, ρ_g/ρ_f, and on the Reynolds number, Re. As the density ratio approaches the unity, the distribution parameter, C_0, should become unity. Based on the limit and various experimental data in fully-developed flows, the distribution parameter was given approximately by

$$C_0 = C_\infty(Re) - \{C_\infty(Re) - 1\}\sqrt{\rho_g / \rho_f}\,, \tag{7}$$

where C_∞ is the asymptotic value of C_0. Here, the density group scales the inertia effects of each phase in a transverse void distribution. Physically, Eq.(7) models the tendency of the lighter phase to migrate into a higher-velocity region, thus resulting in a higher void concentration in the central region [31]. For a laminar flow, C_∞ is 2, but due to the large velocity gradient, C_0 is very sensitive to $<\alpha>$ at low void fractions [31].

Based on a wide range of Reynolds number, Ishii [31] approximated C_∞ to be 1.2 for a flow in a round tube [31]. Thus, for a fully-developed turbulent bubbly flow in a round tube,

$$C_0 \cong 1.2 - 0.2\sqrt{\rho_g / \rho_f}\,. \tag{8}$$

Recently, Hibiki and Ishii [32] suggested that the constitutive equation for the distribution parameter given by Eq.(8) might not give a good prediction in the bubbly-flow regime. Wall peaking in void fraction distribution tends to decrease the distribution parameter considerably. In the mid-1970s, very few databases on local flow parameters were available and, therefore, it might be very difficult to include such local phenomena in the final constitutive equation. As local flow measurement techniques such as double-sensor conductivity probe method and hotfilm anemometry have been developed, databases of local flow parameters for gas and liquid phases in the bubbly flow have been developed extensively.

This enabled reassessment of the constitutive equations for the distribution parameter and the drift velocity by using the local flow parameters such as void fraction, gas velocity, and liquid velocity. Hibiki and Ishii [32] modified the constitutive equation for the distribution parameter, Eq.(8), based on bubble migration dynamics in a flow field. Detailed discussion on the bubbly dynamics suggested that a key parameter determining the phase distribution pattern would be a bubble diameter, and Hibiki and Ishii [32] proposed the following simple correlation as:

$$C_0 = \left(1.2 - 0.2\sqrt{\rho_g / \rho_f}\right)\left(1 - e^{-22\langle D_{Sm}\rangle / D}\right). \tag{9}$$

Equation (9) indicates the significance of the developing void profile in the region given by $0 < \langle D_{Sm}\rangle / D < 0.2$; beyond this region, the values of C_0 approaches rapidly to that for a core peak. The modified correlation of the distribution parameter, Eq.(9), agreed with the distribution parameters determined by local flow parameters of fully-developed turbulent bubbly-flow in round tubes with an average relative deviation of ±6.7 %. The applicability of Eq.(9) was confirmed for 115 data sets taken under the experimental conditions such as $0.262 \text{ m/s} \le \langle j_f \rangle \le 5.00 \text{ m/s}$, $25.4 \text{ mm} \le D \le 60.0 \text{ mm}$, and $1.40 \text{ mm} \le \langle D_{Sm} \rangle$. The detailed discussion and derivation of Eq.(9) can be found in the previous paper [32].

Figure 15 shows the comparison of Eq.(9) with the distribution parameters calculated directly by Eq.(5) with local void fraction, and local superficial gas and liquid velocities. Here, to apply Eq.(9) to bubbly flow in an annulus, hydraulic equivalent diameter, D_H, was used as a channel diameter in Eq.(9). As shown in Fig.15, Eq.(9) gave reasonably good predictions of the distribution parameter and dependence of the distribution parameter on the Sauter mean diameter. An averaged relative deviation between Eq.(9) and experimental distribution parameter is estimated to be ±10.2 %. This suggests that Eq.(9) may be applicable even to bubbly flow in an annulus.

For a practical use, the Sauter mean diameter in Eq.(9) should be correlated with easily measurable quantities such as superficial gas and liquid velocities. Recently, Hibiki and Ishii [33] developed new correlation of the interfacial area concentration under steady fully-developed bubbly flow conditions based on the interfacial area transport equation as follows:

$$\left\langle \widetilde{D}_{Sm} \right\rangle = 1.99 \widetilde{Lo}^{-0.335} \left\langle \widetilde{\varepsilon} \right\rangle^{-0.0796}, \tag{10}$$

where $Lo \equiv \sqrt{\dfrac{\sigma}{g\Delta\rho}}$, $\left\langle \widetilde{D}_{Sm} \right\rangle \equiv \dfrac{\left\langle D_{Sm} \right\rangle}{Lo}$, $\widetilde{Lo} \equiv \dfrac{Lo}{D_H}$ and $\left\langle \widetilde{\varepsilon} \right\rangle \equiv Lo \left(\dfrac{\left\langle \varepsilon \right\rangle}{\nu_f^3} \right)^{1/4}$.

The energy dissipation rate per unit mass in Eq.(10) can be simply calculated from the mechanical energy equation as [33]:

$$\left\langle \varepsilon \right\rangle = g \left\langle j_g \right\rangle \exp\left(-ARe_f\right) + \frac{\left\langle j \right\rangle}{\rho_m} \left(-\frac{dP}{dz} \right)_F \left\{ 1 - \exp\left(-ARe_f\right) \right\}, \tag{11}$$

where g, A, Re_f, ρ_m, and $(-dP/dz)_F$ refer to the gravitational acceleration, a coefficient (=0.0005839), Reynolds number of the liquid phase defined by $\langle j_f \rangle D_H / \nu_f$, the mixture density, and the pressure loss per unit length due to friction, respectively. The pressure loss per unit length due to friction can be calculated from Lockhart-Martinelli's correlation [34]. Equation (11) suggests that as the liquid flow rate decreases or increases, the energy dissipation rate per unit mass asymptotically approaches to the energy dissipation rate per unit mass due to bubble expansion or wall friction, respectively. The above Sauter mean diameter correlation, Eq.(10), agreed with 459 data sets measured in bubble columns and forced convective bubbly flows under various conditions. These data sets covered extensive loop and flow conditions such as channel geometry (circular or rectangular channel), channel hydraulic equivalent diameter (9.0 mm ~ 5500 mm), flow direction (vertical or horizontal flow), superficial gas velocity (0.000788 m/s ~ 4.87 m/s), and superficial liquid velocity (0.00

m/s ~ 6.55 m/s). The extensive database also covered wide ranges of physical properties such as liquid density (684 kg/m^3 ~ 1594 kg/m^3), liquid viscosity (0.410 mPa･s ~ 21.1 mPa･s), and surface tension (20.0 mN/m ~ 75.0 mN/m). An excellent agreement was obtained between the developed semi-theoretical correlation and 459 data within an average relative deviation of ±22.0 %.

Figure 16 shows the comparison of Eq.(10) with the Sauter mean diameters calculated directly by Eq.(10) with local void fraction, and local superficial gas and liquid velocities. Equation (10) gave reasonably good predictions of the Sauter mean diameter. An averaged relative deviation between Eq.(10) and experimental distribution parameter is estimated to be ±9.65 %. This suggests that Eq.(10) may be applicable even to bubbly flow in an annulus.

3.2.3. Constitutive equation of drift velocity in bubbly flow

Ishii [31] also developed a simple correlation for the drift velocity in bubbly-flow regime. In the distorted-fluid-particle regime, the single particle drag coefficient, $C_{D\infty}$, depends only on the particle radius and fluid properties and not on the velocity or the viscosity. Thus, for a particle of a fixed diameter, $C_{D\infty}$ becomes constant. In considering the drag coefficient, C_D, for a multi-particle system with the same radius, it is necessary to take into account the restrictions imposed by the existence of other particles on the flow field. Therefore, C_D is expected to be different from $C_{D\infty}$, in this regime. Because of the wake characteristic of the turbulent eddies and particle motions, a particle sees the increased drag due to other particles in essentially similar ways as in the Newton's regime for a solid-particle system, where $C_{D\infty}$ is also constant under a wake turbulent flow condition. Hence, Ishii [31] postulated that regardless of the differences in $C_{D\infty}$ in these regimes, the effect of increased

drag in the distorted-fluid-particle regime could be predicted by the similar expression as that in the Newton's regime. In other words, Ishii [31] assumed that $C_D/C_{D\infty}$ for the distorted particle regime would be the same as that in the Newton's regime. Under this assumption, local drift velocity, v_{gj}, for the distorted-fluid-particle or bubbly flow can be obtained as [31]:

$$v_{gj} = \sqrt{2}\left(\frac{g\sigma\Delta\rho}{\rho_f^2} \right)^{1/4} (1-\alpha)^{1.75} \quad \text{for } \mu_f >> \mu_g \,. \tag{12}$$

where σ, $\Delta\rho$, μ_f and μ_g are the surface tension, the density difference between phases, the liquid viscosity and the gas viscosity, respectively. The calculation of void-fraction-weighted mean of local drift velocity, V_{gj}, based on the local constitutive equation is the integral transformation; Eq.(6); thus it will require additional information on the void profile. Since this profile is not known in general, we make the following simplifying approximations. The average drift velocity V_{gj} due to the local slip can be predicted by the same expression as the local constitutive relation [31], provided the local void fraction and the non-dimensional difference of the stress gradient are replaced by average values. These approximations are good for flows with a relatively flat void fraction profile; also, they can be considered acceptable from the overall simplicity of the one-dimensional model.

For a fully-developed vertical flow, the stress distribution in the fluid and in the dispersed phase should be similar; thus the effect of shear gradient on the mean local drift velocity can be neglected. Under these conditions we obtain the following results:

$$V_{gj} = \sqrt{2}\left(\frac{g\sigma\Delta\rho}{\rho_f^2} \right)^{1/4} (1-\langle\alpha\rangle)^{1.75} \quad \text{for } \mu_f >> \mu_g \,. \tag{13}$$

The contribution of the drift velocity to the gas velocity would be rather small for flow regimes such as slug, churn, and annular flow regimes, whereas it would be significant

for bubbly flow regime. Thus, it may be important to reevaluate the constitutive equation for drift velocity in the bubbly flow given by Ishii [31], Eq.(13), with the drift velocities determined from local flow parameters measured in this experiment. Figure 17 shows the comparison of Eq.(13) with the drift velocities determined directly from local flow parameters measured in the experiment. In this figure, solid line indicates the drift velocities calculated by Eq.(6). The estimation error of the void-fraction-weighted mean drift velocity would mainly be attributed to the measurement error of the relative velocity between phases, which can be calculated by subtracting the liquid velocity from the gas velocity. When the measurement errors for gas and liquid velocities are ±10 %, the uncertainty in the void-fraction-weighted mean drift velocity can roughly be estimated to be ±40 % and ±80 % for the gas velocities of 0.50 and 1.0 m/s, respectively, from the error propagation. Here, the void-fraction-weighted drift velocity is assumed to be 0.25 m/s in the error estimation by conservative estimate. Thus, it would be very difficult to make a quantitative discussion based on the data for $<j_f>\geq 1.0$ m/s due to considerably large error. Therefore, the data for $<j_f>\geq 1.0$ m/s are not shown in the figure.

As can be clearly seen from Fig.17, the void-fraction-weighted mean drift velocity appears to decrease with the increase in void fraction. The drift velocity correlation developed by Ishii [31], Eq.(13), can represent this tendency marvelously. Taking account of large error in experimental drift velocity, it can be concluded that Eq.(13) can give the proper trend of the drift velocity of bubbly flow regime against the void fraction as well as good predictions of the values of the drift velocities in bubbly flow regime. Thus, Eq.(13) can be applicable to bubbly flow in an annulus.

4. Conclusions

Local measurements of flow parameters were performed for vertical upward bubbly flows in an annulus. The annulus channel consisted of an inner rod with a diameter of 19.1 mm and an outer round tube with an inner diameter of 38.1 mm, and the hydraulic equivalent diameter was 19.1 mm. Double-sensor conductivity probe was used for measuring void fraction, interfacial area concentration, and interfacial velocity, and Laser Doppler anemometer was utilized for measuring liquid velocity and turbulence intensity. A total of 20 data sets for void fraction, interfacial area concentration, and interfacial velocity were acquired consisting of five void fractions, about 0.050, 0.10, 0.15, 0.20, and 0.25, and four superficial liquid velocities, 0.272, 0.516, 1.03, and 2.08 m/s. A total of 8 data sets for liquid velocity and turbulence intensity were acquired consisting of five void fractions, about 0.050, and 0.10, and four superficial liquid velocities, 0.272, 0.516, 1.03, and 2.08 m/s. The mechanisms to form the radial profiles of local flow parameters were discussed in detail. The constitutive equations for distribution parameter and drift velocity in the drift-flux model, and the semi-theoretical correlation for Sauter mean diameter namely interfacial area concentration, which were proposed previously, were validated by local flow parameters obtained in the experiment using the annulus.

Acknowledgments

The authors wish to thank Dr. Sun (Purdue University, USA) for his devoted assistance and discussion in the LDA measurement. The research project was supported by the Tokyo Electric Power Company (TEPCO). The authors would like to express their sincere appreciation for the support and guidance from Dr. Mori of the TEPCO.

References

[1] A. Serizawa, I. Kataoka, 1988. Phase distribution in two-phase flow, Transient Phenomena in Multiphase Flow, Hemisphere Publishing Corporation (1988) pp.179-224.

[2] T. J. Liu, Experimental investigation of turbulence structure in two-phase bubbly flow, Ph D. Thesis, Northwestern University, USA (1989).

[3] A. Serizawa, I. Kataoka, I. Michiyoshi, Phase distribution in bubbly flow, Multiphase Science and Technology (Eds. G. F. Hewitt, J. M. Delhaye, and N. Zuber), Hemisphere Publishing Corporation, vol.6 (1991) pp.257-301.

[4] S. Kalkach-Navarro, The mathematical modeling of flow regime transition in bubbly two-phase flow. Ph D. Thesis, Rensselaer Polytechnic Institute, USA (1992).

[5] G. Kocamustafaogullari, W. D. Huang, J. Razi, Measurement of modeling of average void fraction, bubble size and interfacial area, Nuclear Engineering and Design 148 (1994) 437-453.

[6] W. H. Leung, S. T. Revankar, Y. Ishii, M. Ishii, Axial development of interfacial area and void concentration profiles measured by double-sensor probe method, International Journal of Heat and Mass Transfer 38 (1995) 445-453.

[7] C. Grossetete, Caracterisation experimentale et simulations de l'evolution d'un ecoulement diphasique a bulles ascendant dans une conduite verticale, Ph D. Thesis, Ecole Centrale Paris, France (1995).

[8] B. J. Yun, Measurement of two-phase flow parameters in the subcooled boiling, Ph D. Thesis, Seoul national University, Korea (1996).

[9] S. Hogsett, M. Ishii, Local two-phase flow measurements using sensor techniques, Nuclear Engineering and Design 175 (1997) 15-24.

[10] T. Hibiki, S. Hogsett, M. Ishii, Local measurement of interfacial area, interfacial velocity and liquid turbulence in two-phase flow, Nuclear Engineering and Design 184 (1998) 287-304.

[11] T. Hibiki, M. Ishii, Experimental study on interfacial area transport in bubbly two-phase flows, International Journal of Heat and Mass Transfer 42 (1999) 3019-3035.

[12] T. Hibiki, M. Ishii, Z. Xiao, Axial interfacial area transport of vertical bubbly flows, International Journal of Heat and Mass Transfer 44 (2001) 1869-1888.

[13] K. Mishima, T. Hibiki, H. Nishihara, Effect of pressure on critical heat flux for water in an internally heated annulus, Nuclear Science Journal 32 (1995) 34-41.

[14] M. D. Bartel, M. Ishii, T. Masukawa, Y. Mi, R. Situ, Interfacial area measurements in subcooled flow boiling, Nuclear Engineering and Design 210 (2001) 135-155.

[15] I. Kataoka, M. Ishii, A. Serizawa, Local formulation and measurements of interfacial area concentration in two-phase flow, International Journal of Multiphase Flow 12 (1986) 505-529.

[16] S. T. Revankar, M. Ishii, Local interfacial area measurement in bubbly flow, International Journal of Heat and Mass Transfer 35 (1992) 913-925.

[17] Q. Wu, M. Ishii, Sensitivity study on double-sensor conductivity probe for the measurement of interfacial area concentration in bubbly flow, International Journal of Multiphase Flow 25 (1999) 155-173.

[18] S. Kim, X. Y. Fu, X. Wang, M. Ishii, Development of the miniaturized four-sensor conductivity probe and the signal processing scheme, International Journal of Heat and Mass Transfer 43 (2000) 4101-4118.

[19] T. Hibiki, W. H. Leung, M. Ishii, Measurement method of local interfacial area in two-phase flow using a double sensor probe, Technical report, PU-NE-97/5, School of Nuclear Engineering, Purdue University, West Lafayette, IN, USA, 1997.

[20] W. H. Leung, C. S. Eberle, Q. Wu, T. Ueno, M. Ishii, Quantitative characterizations of phasic structure developments by local measurement methods in two-phase flow, Proceedings of the 2nd International Conference on Multiphase Flow '95 – Kyoto, Japan (1995) pp.IN2-17-IN2-25.

[21] M. Ishii, N. Zuber, Drag coefficient and relative velocity in bubbly, droplet or particulate flows, AIChE Journal 25 (1979) 843-855.

[22] X. Sun, T. Smith, S. Kim, M. Ishii, Local measurement of liquid velocity in bubbly flow, Proceedings of the 8th International Conference on Nuclear Engineering, No. ICONE-8476, (2000).

[23] M. Ishii, Y. Mi, R. Situ, T. Hibiki, Experimental and theoretical investigation of subcooled boiling for numerical simulation Progress report 4, Technical report, PU-NE-01/7, School of Nuclear Engineering, Purdue University, West Lafayette, IN, USA, 2001.

[24] M. Ishii, Y. Mi, R. Situ, T. Masukawa, Experimental and theoretical investigation of subcooled boiling for numerical simulation Progress report 1, Technical report, PU-NE-00/6, School of Nuclear Engineering, Purdue University, West Lafayette, IN, USA, 2000.

[25] K. Sekoguchi, T. Sato, T. Honda, Two-phase bubbly flow (first report), Transactions of JSME 40 (1974) 1395-1403 (in Japanese).

[26] I. Zun, Transition from wall void peaking to core void peaking in turbulent bubbly flow, in : N. H. Afgan (Ed.), Transient Phenomena in Multiphase Flow, Hemisphere, Washington, DC, 1988, pp.225-245.

[27] Y. Taitel, D. Bornea, E. A. Dukler, Modelling flow pattern transitions for steady upward gas-liquid flow in vertical tubes, AIChE Journal 26 (1980) 345-354.

[28] A. Serizawa, I. Kataoka, Turbulence suppression in bubbly two-phase flow, Nuclear Engineering and Design 122 (1990) 1-16.

[29] S. Wang, S. Lee, O. C. Jones, Jr., R. T. Lahey, Jr., 3-D turbulence structure and phase distribution measurements in bubbly two-phase flows, International Journal of Multiphase Flow 13 (1987) 327-343.

[30] I. Michiyoshi, A. Serizawa, Turbulence in two-phase bubbly flow, Nuclear Engineering and Design 95 (1986) 253-257.

[31] M. Ishii, One-dimensional drift-flux model and constitutive equations for relative motion between phases in various two-phase flow regimes, ANL-77-47, USA, 1977.

[32] T. Hibiki, M. Ishii, Distribution parameter and drift velocity of drift-flux model in bubbly flow, International Journal of Heat and Mass Transfer 45 (2002) 707-721.

[33] T. Hibiki, M. Ishii, Interfacial area concentration of bubbly flow systems, Chemical Engineering Science (accepted).

[34] R. W. Lockhart, R. C. Martinelli, Proposed correlation of data for isothermal two-phase two-component flow in pipes, Chemical Engineering Progress 5 (1949) 39-48.

Local Flow Measurements of Vertical Upward Bubbly Flow in an Annulus

Takashi Hibiki, Rong Situ, Ye Mi, Mamoru Ishii

Caption of Table

Table 1. Flow conditions in this experiment.

Captions of Figures

Fig.1. Laser Doppler anemometry (Dual beam approach).
(Courtesy of TSI Inc., St. Paul, Minnesota)

Fig.2. Integrated 1-component fiber optic LDA system.
(Courtesy of TSI Inc., St. Paul, Minnesota)

Fig.3. Determining of LDA measuring positions.

Fig.4. Schematic diagram of experimental loop.

Fig.5. Effect of seeding particles on flow parameters.

Fig.6. Local void fraction profiles at z/D_H=51.0.

Fig.7. Local interfacial area concentration profiles at z/D_H=51.0.

Fig.8. Local interfacial velocity profiles at z/D_H=51.0.

Fig.9. Local Sauter mean diameter profiles at z/D_H=51.0.

Fig.10. Dependence of peak void fraction and radial position on void fraction and superficial liquid velocity.

Fig.11. Maps of phase distribution patterns.

Fig.12. Dependence of interfacial velocity profile on void fraction and superficial liquid velocity.

Fig.13. Local liquid velocity profiles at z/D_H=51.0.

Fig.14. Local turbulence intensity profiles at z/D_H=51.0.

Fig.15 Comparison of constitutive equation for distribution parameter in bubbly flow regime with distribution parameters determined experimentally.

Fig.16 Comparison of semi-theoretical correlation for Sauter mean diameter with Sauter mean diameters determined experimentally.

Fig.17 Comparison of constitutive equation for drift velocity in bubbly flow regime with drift velocities determined experimentally.

Table 1 Flow conditions in this experiment.

Symbols	●	▲	■	▼	◆
$\langle j_f \rangle$ [m/s]	$\langle j_{g,N} \rangle$ [m/s]	$\langle j_{g,N} \rangle$ [m/s]	$\langle j_{g,N} \rangle$ [m/s]	$\langle j_{g,N} \rangle$ [m/s]	$\langle j_{g,N} \rangle$ [m/s]
0.272	0.0313	0.0506	0.0690	0.0888	0.105
0.516	0.0406	0.0687	0.103	0.135	0.176
1.03	0.0683	0.130	0.201	0.400	0.489
2.08	0.108	0.215	0.505	0.651	0.910

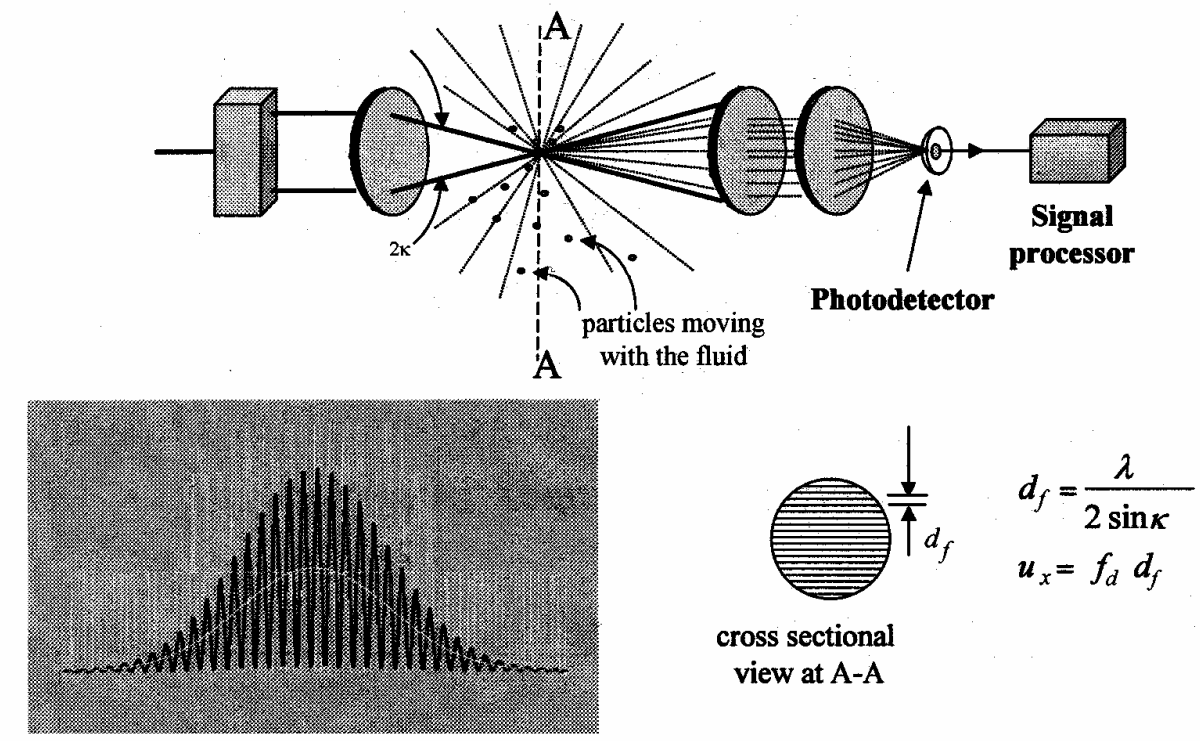
A
2κ
A
particles moving
with the fluid
Photodetector
Signal
processor
d_f
cross sectional
view at A-A
$d_f = \frac{\lambda}{2 \sin \kappa}$
$u_x = f_d \, d_f$

Fig.1

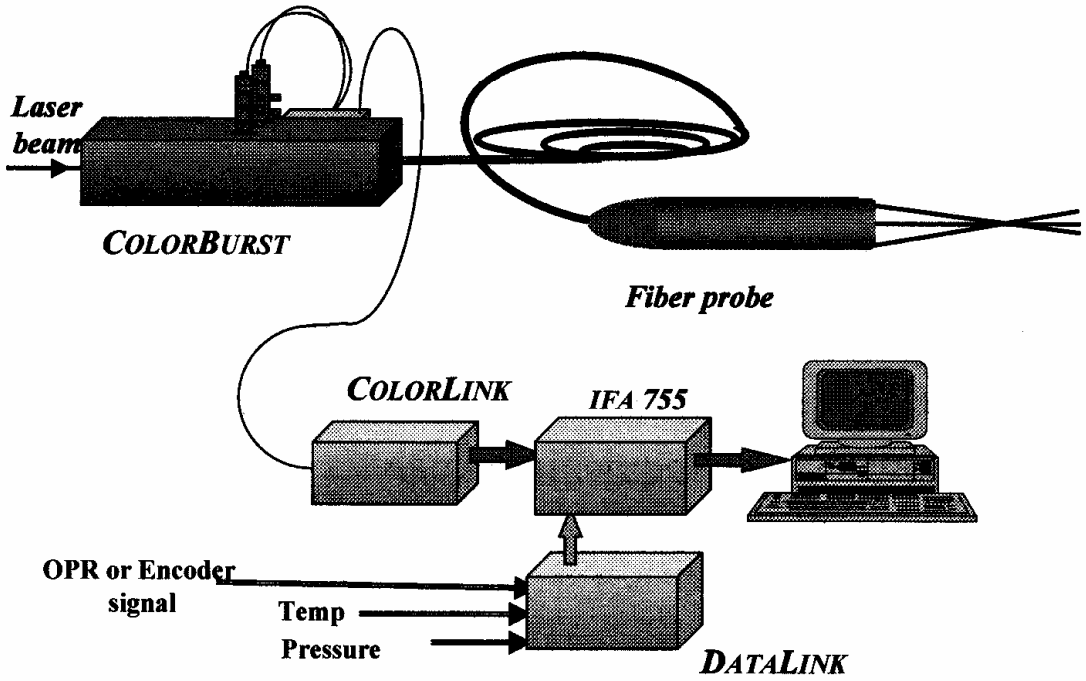
Laser
beam
COLORBURST
Fiber probe
COLORLINK
IFA 755
OPR or Encoder
signal
Temp
Pressure
DATALINK

Fig.2

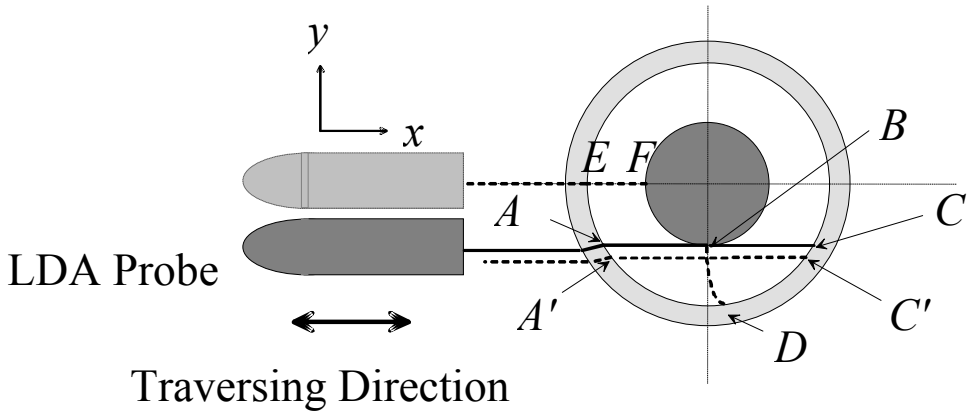

(a) Top View of the Test Section

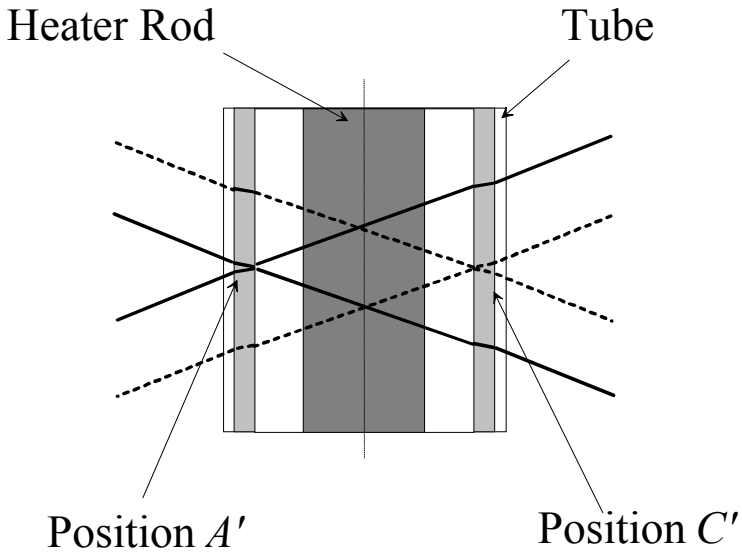

(b) Side View of the Test Section

Fig.3

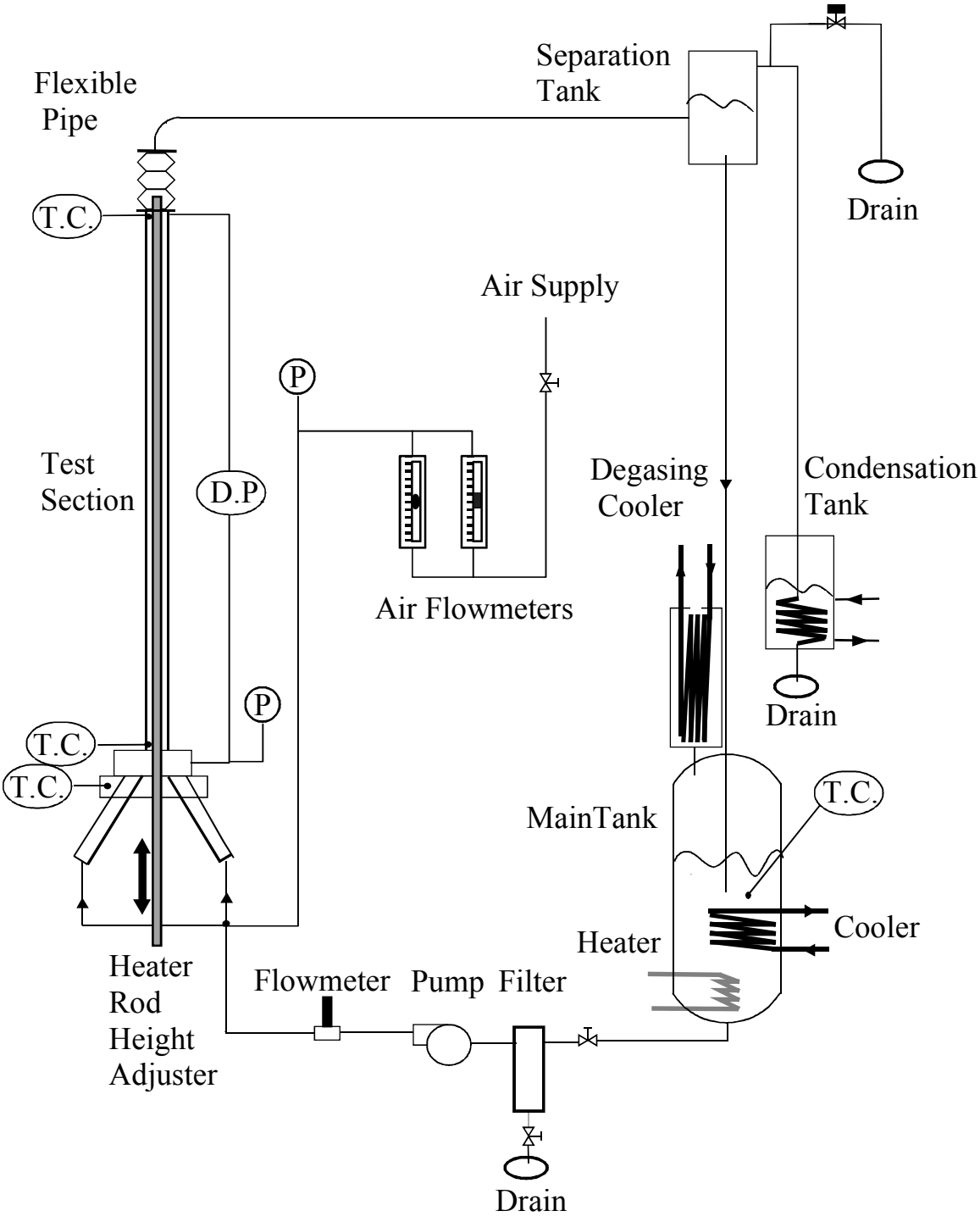
Flexible
Pipe
Separation
Tank
Drain
T.C.
Air Supply
P
Test
Section
D.P
Degasing
Cooler
Condensation
Tank
Air Flowmeters
Drain
P
T.C.
T.C.
MainTank
T.C.
Heater
Cooler
Heater
Rod
Height
Adjuster
Flowmeter
Pump
Filter
Drain

Fig.4

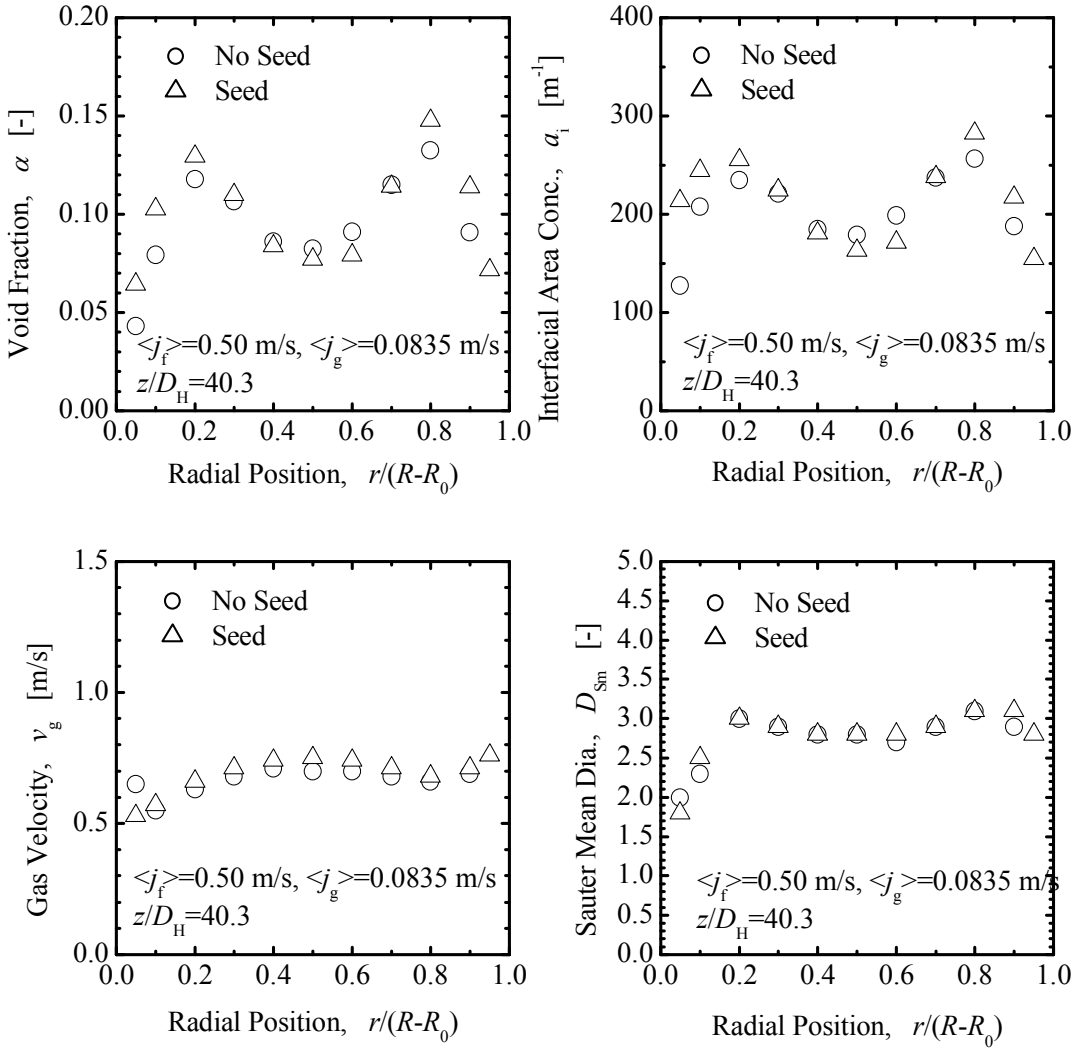
Void Fraction, α [-]
Interfacial Area Conc., a_i [m^{-1}]
Gas Velocity, v_g [m/s]
Sauter Mean Dia., D_{Sm} [-]
Radial Position, $r/(R-R_0)$
No Seed
Seed
<j_f>=0.50 m/s, <j_g>=0.0835 m/s
z/D_H=40.3

Fig.5

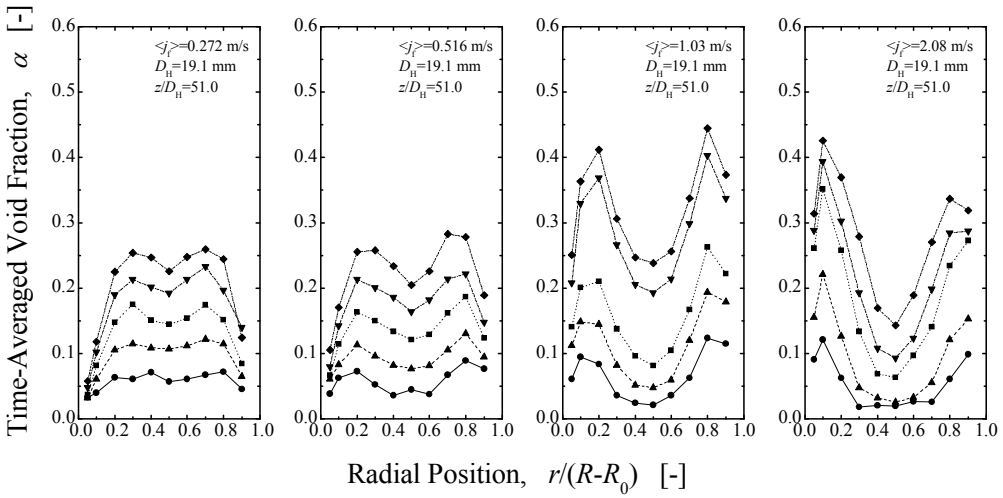
Time-Averaged Void Fraction, α [-]
<j_f>=0.272 m/s
D_H=19.1 mm
z/D_H=51.0
<j_f>=0.516 m/s
D_H=19.1 mm
z/D_H=51.0
<j_f>=1.03 m/s
D_H=19.1 mm
z/D_H=51.0
<j_f>=2.08 m/s
D_H=19.1 mm
z/D_H=51.0
Radial Position, $r/(R-R_0)$ [-]

Fig.6

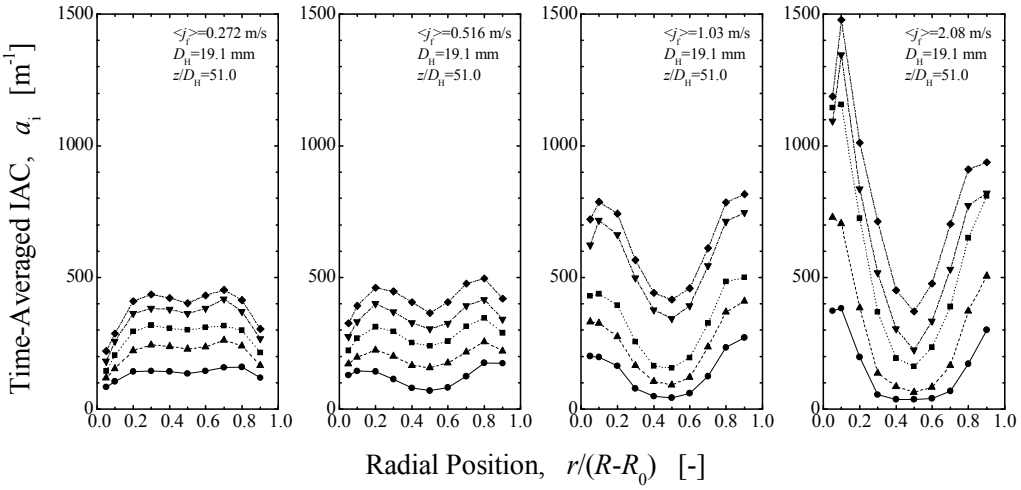
Time-Averaged IAC, a_i [m^{-1}]
Radial Position, $r/(R-R_0)$ [-]
<j_f>=0.272 m/s
<j_f>=0.516 m/s
<j_f>=1.03 m/s
<j_f>=2.08 m/s
D_H=19.1 mm
z/D_H=51.0
0
500
1000
1500
0.0 0.2 0.4 0.6 0.8 1.0

Fig.7

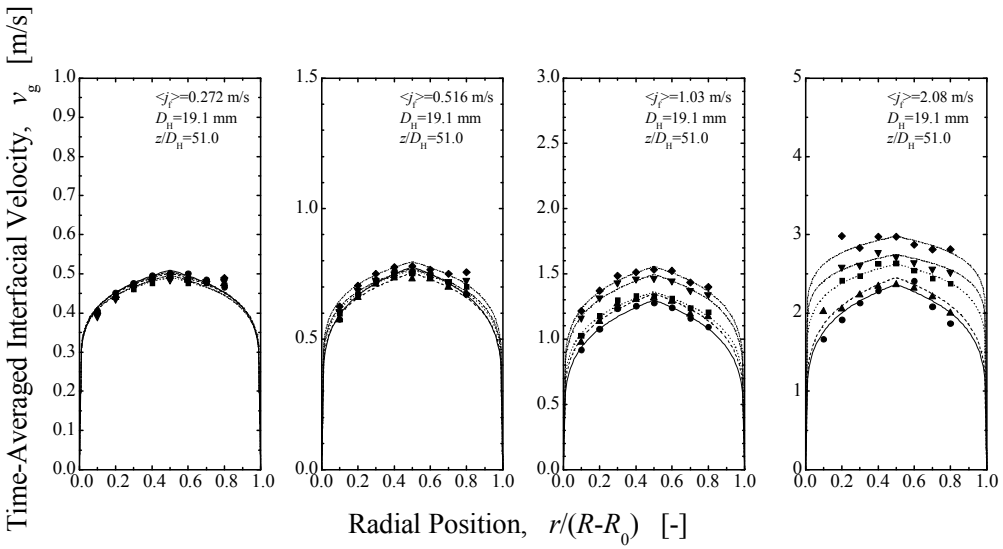
Time-Averaged Interfacial Velocity, v_g [m/s]
$\langle j_f \rangle$=0.272 m/s
D_H=19.1 mm
z/D_H=51.0
$\langle j_f \rangle$=0.516 m/s
D_H=19.1 mm
z/D_H=51.0
$\langle j_f \rangle$=1.03 m/s
D_H=19.1 mm
z/D_H=51.0
$\langle j_f \rangle$=2.08 m/s
D_H=19.1 mm
z/D_H=51.0
Radial Position, $r/(R-R_0)$ [-]

Fig.8

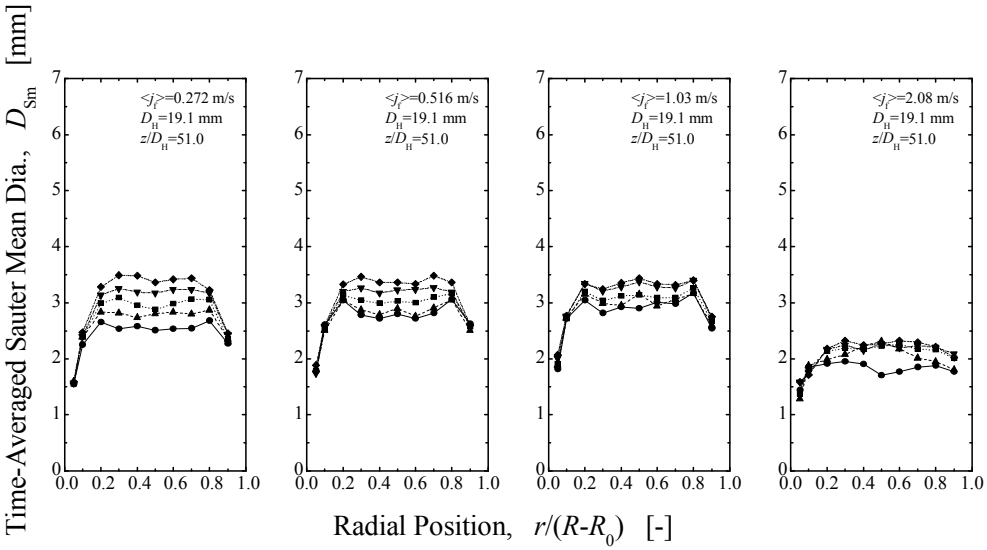
Time-Averaged Sauter Mean Dia., D_{Sm} [mm]
$<j_f>$=0.272 m/s
D_H=19.1 mm
z/D_H=51.0
$<j_f>$=0.516 m/s
D_H=19.1 mm
z/D_H=51.0
$<j_f>$=1.03 m/s
D_H=19.1 mm
z/D_H=51.0
$<j_f>$=2.08 m/s
D_H=19.1 mm
z/D_H=51.0
Radial Position, $r/(R-R_0)$ [-]

Fig.9

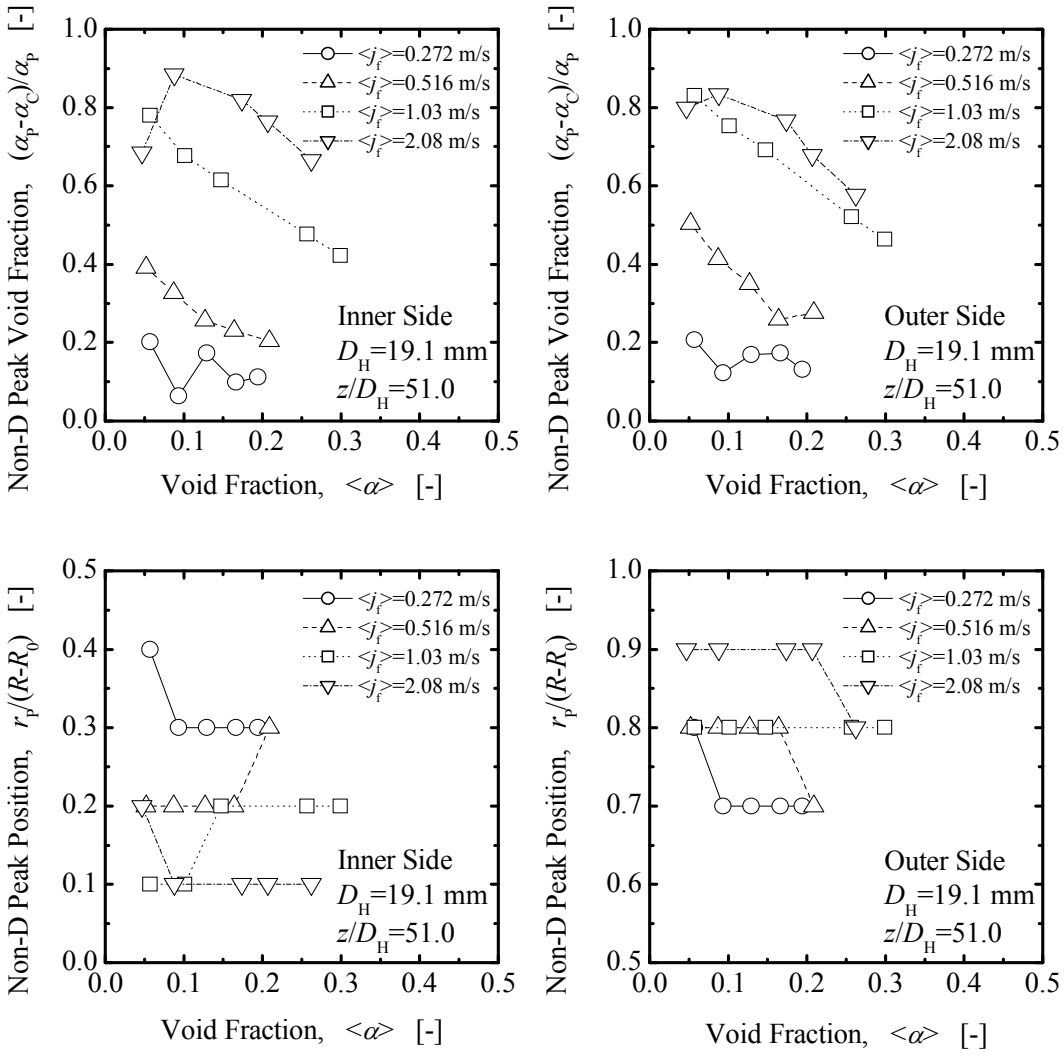
Non-D Peak Void Fraction, $(\alpha_P-\alpha_C)/\alpha_P$ [-]
Void Fraction, $<\alpha>$ [-]
$<j_f>$=0.272 m/s
$<j_f>$=0.516 m/s
$<j_f>$=1.03 m/s
$<j_f>$=2.08 m/s
Inner Side
D_H=19.1 mm
z/D_H=51.0
Outer Side
D_H=19.1 mm
z/D_H=51.0
Non-D Peak Position, $r_p/(R-R_0)$ [-]
Inner Side
D_H=19.1 mm
z/D_H=51.0
Outer Side
D_H=19.1 mm
z/D_H=51.0

Fig.10

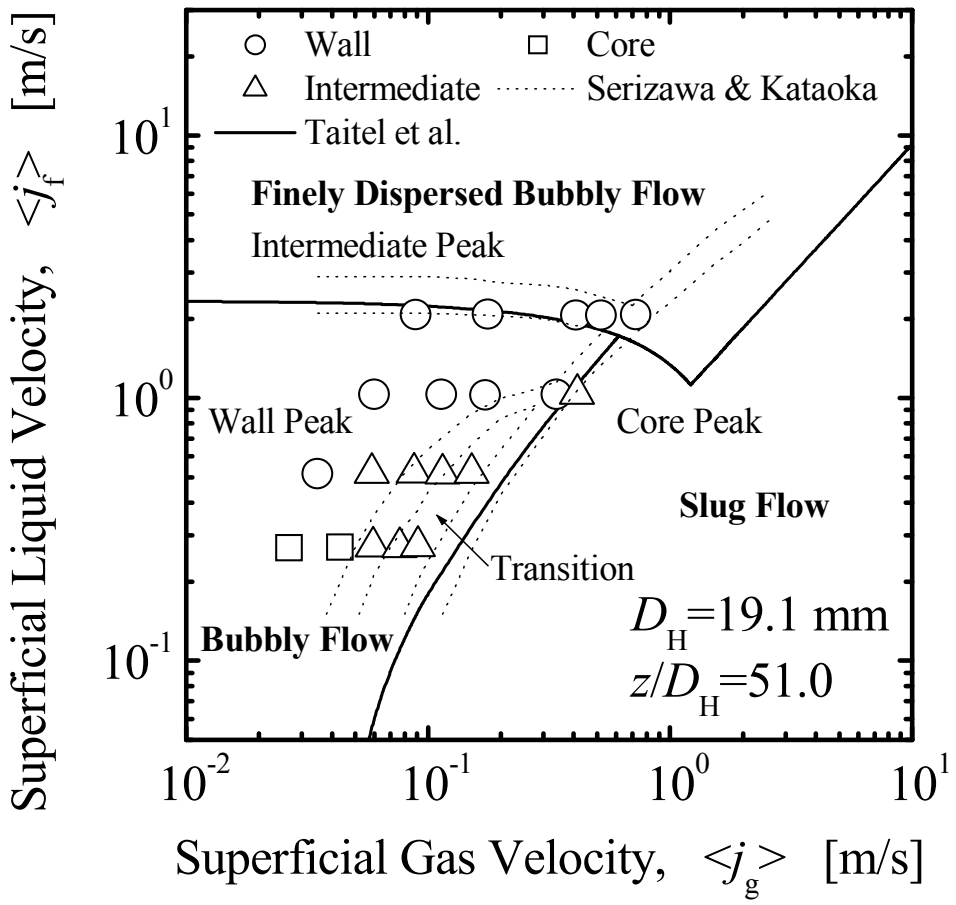
Wall
Core
Intermediate
Serizawa & Kataoka
Taitel et al.
Finely Dispersed Bubbly Flow
Intermediate Peak
Wall Peak
Core Peak
Slug Flow
Transition
Bubbly Flow
D_H=19.1 mm
z/D_H=51.0
Superficial Liquid Velocity, $<j_f>$ [m/s]
Superficial Gas Velocity, $<j_g>$ [m/s]
10^1
10^0
10^{-1}
10^{-2}
10^{-1}
10^0
10^1

Fig.11

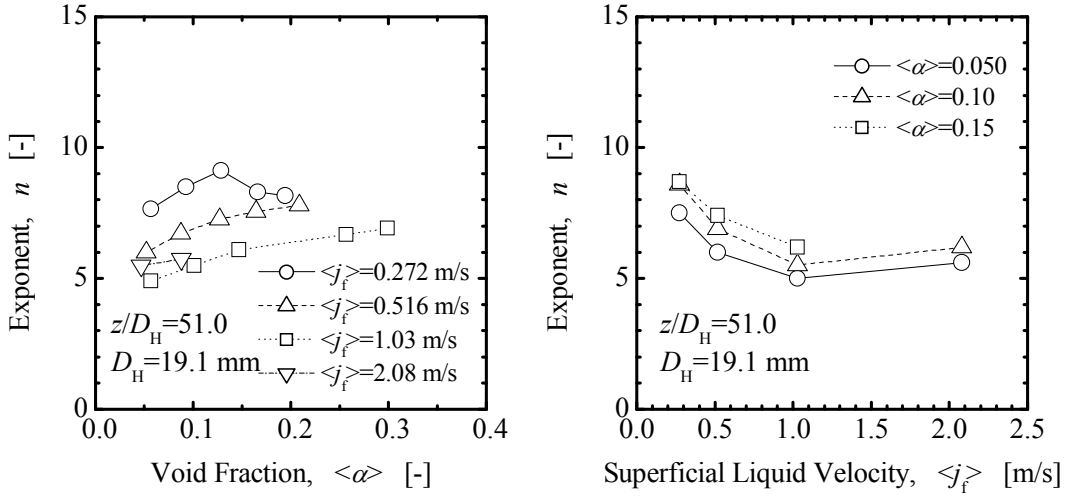
Exponent, n [-]
Void Fraction, <α> [-]
z/D_H=51.0
D_H=19.1 mm
<j_f>=0.272 m/s
<j_f>=0.516 m/s
<j_f>=1.03 m/s
<j_f>=2.08 m/s
Exponent, n [-]
Superficial Liquid Velocity, <j_f> [m/s]
z/D_H=51.0
D_H=19.1 mm
<α>=0.050
<α>=0.10
<α>=0.15

Fig.12

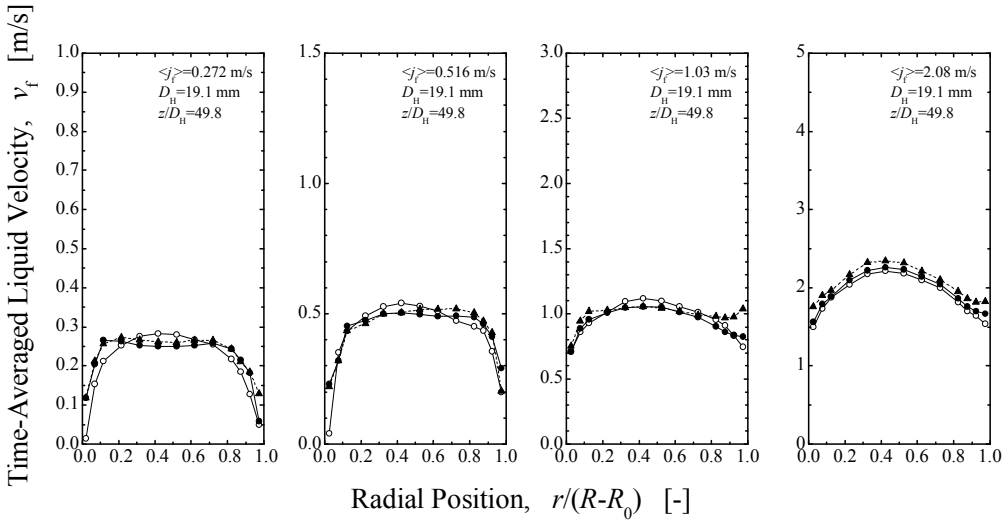
Time-Averaged Liquid Velocity, v_f [m/s]
$\langle j_f \rangle$=0.272 m/s
D_H=19.1 mm
z/D_H=49.8
$\langle j_f \rangle$=0.516 m/s
D_H=19.1 mm
z/D_H=49.8
$\langle j_f \rangle$=1.03 m/s
D_H=19.1 mm
z/D_H=49.8
$\langle j_f \rangle$=2.08 m/s
D_H=19.1 mm
z/D_H=49.8
Radial Position, $r/(R-R_0)$ [-]

Fig.13

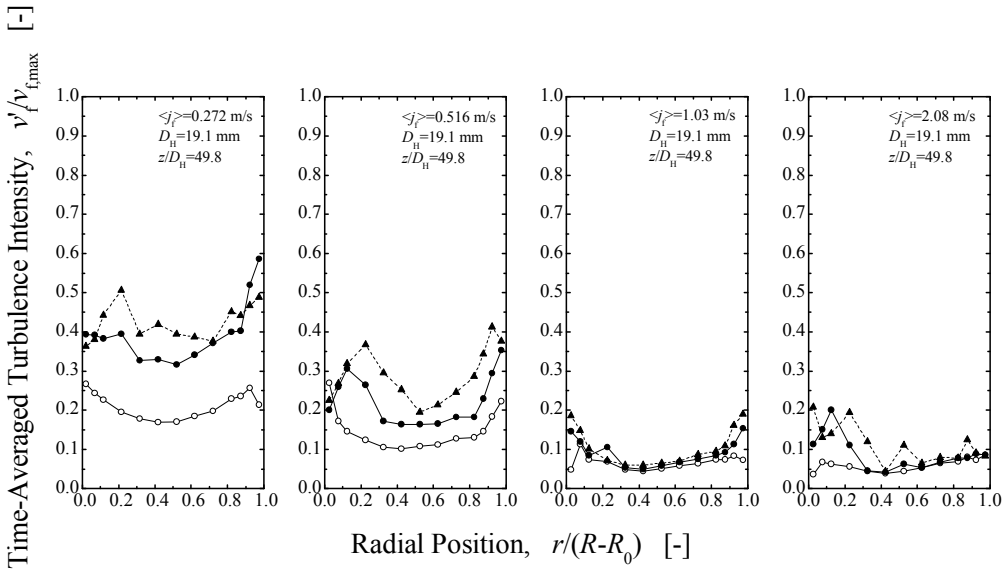
Time-Averaged Turbulence Intensity, $v_f'/v_{f,max}$ [-]
$<j_f>$=0.272 m/s
D_H=19.1 mm
z/D_H=49.8
$<j_f>$=0.516 m/s
D_H=19.1 mm
z/D_H=49.8
$<j_f>$=1.03 m/s
D_H=19.1 mm
z/D_H=49.8
$<j_f>$=2.08 m/s
D_H=19.1 mm
z/D_H=49.8
Radial Position, $r/(R-R_0)$ [-]

Fig.14

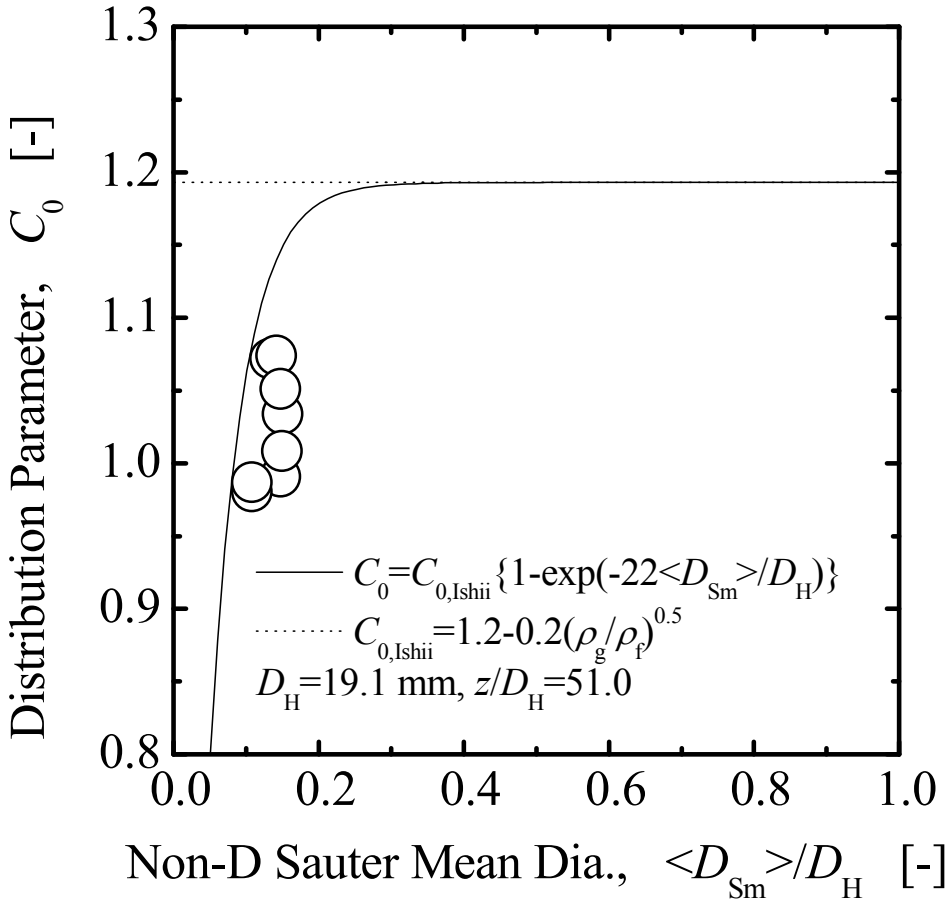
1.3
1.2
1.1
1.0
0.9
0.8
0.0
0.2
0.4
0.6
0.8
1.0
Distribution Parameter, C_0 [-]
Non-D Sauter Mean Dia., $<D_{Sm}>/D_H$ [-]
$C_0=C_{0,Ishii}\{1-\exp(-22<D_{Sm}>/D_H)\}$
$C_{0,Ishii}=1.2-0.2(\rho_g/\rho_f)^{0.5}$
D_H=19.1 mm, z/D_H=51.0

Fig.15

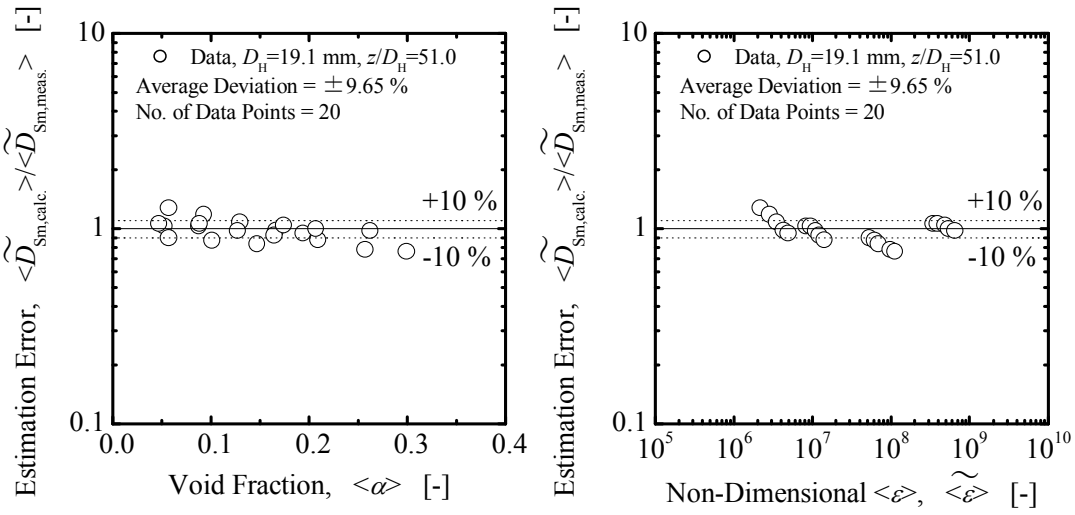
Data, D_H=19.1 mm, z/D_H=51.0
Average Deviation = ±9.65 %
No. of Data Points = 20
+10 %
-10 %
Estimation Error, $\langle \tilde{D}_{Sm,calc.} \rangle / \langle \tilde{D}_{Sm,meas.} \rangle$ [-]
Void Fraction, $\langle \alpha \rangle$ [-]
Non-Dimensional $\langle \varepsilon \rangle$, $\langle \tilde{\varepsilon} \rangle$ [-]

Fig.16

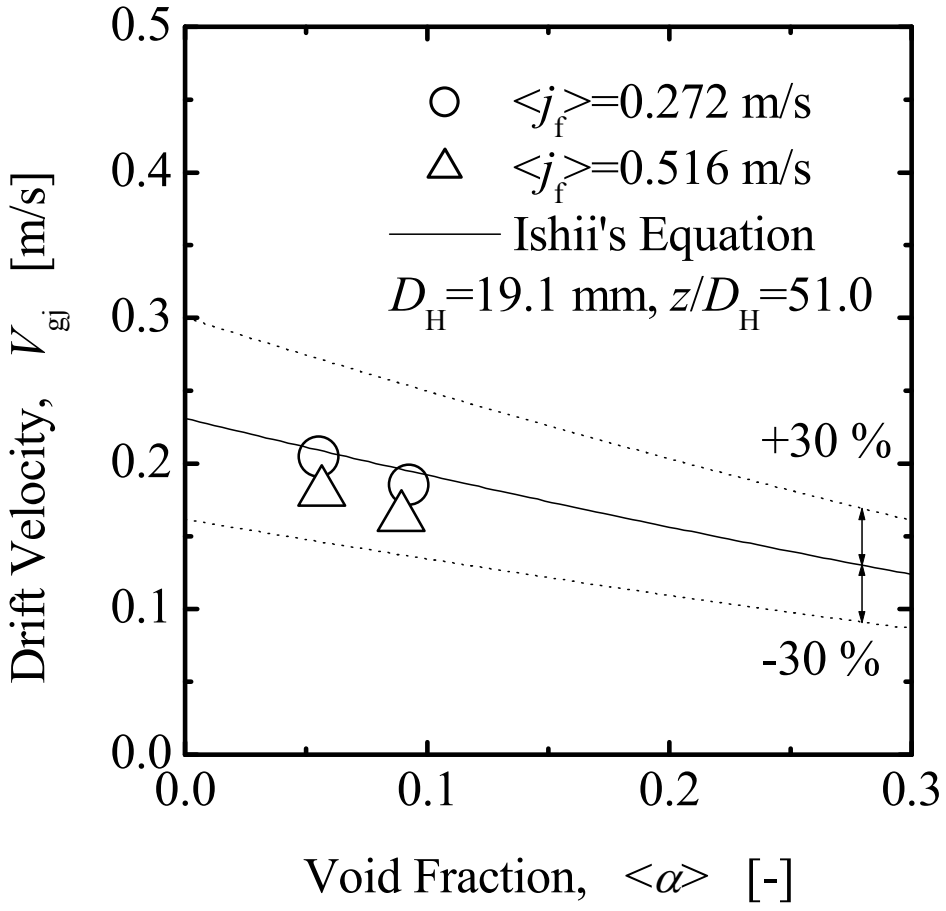
0.5
0.4
0.3
0.2
0.1
0.0
0.0
0.1
0.2
0.3
Drift Velocity, V_{gj} [m/s]
Void Fraction, <α> [-]
○ <j_f>=0.272 m/s
△ <j_f>=0.516 m/s
Ishii's Equation
D_H=19.1 mm, z/D_H=51.0
+30 %
-30 %

Fig.17